

Master's thesis

Development and application of near-infrared spectroscopy for the detection of atmospheric pollutants and volatile compounds of agri-food products

Giorgos Stavrakakis

Department of Materials Science and Technology
University of Crete

Scientific committee

Prof. D. Papazoglou (Supervisor)
Dr. M. Velegrakis (Co-supervisor)
Dr. P. Samartzis

Heraklion, 2022

Table of Contents

<i>Acknowledgements</i>	2
<i>Abstract</i>	3
<i>1.Introduction</i>	4
<i>2.Theory</i>	6
<i>2.1. Near-Infrared Spectroscopy</i>	6
<i>2.1.1 Harmonic Oscillator</i>	6
<i>2.1.2 Anharmonic Oscillator</i>	9
<i>2.1.3 NIR Spectra</i>	10
<i>2.1.4 Number of vibrational modes</i>	11
<i>2.2 Tunable Diode Laser Absorption Spectroscopy (TDLAS)</i>	11
<i>2.3 Tunable Diode Laser Photoacoustic spectroscopy(TDLPAS)</i>	14
<i>2.3.1 The Photoacoustic Effect</i>	14
<i>2.3.2 Nonradiative transitions and photoacoustic signal generation</i>	14
<i>2.3.3 Relaxation processes and heat release</i>	15
<i>2.3.4 Photoacoustic signal generation in gases – The governing equations</i>	16
<i>3. Materials, Methods and Instrumentation</i>	18
<i>Experimental Setups</i>	18
<i>3.1 TDLAS Experimental Setup and Method</i>	18
<i>3.2 TDLPAS Experimental Setup and Method</i>	20
<i>3.3 Hybrid TDLAS-TDLPAS Experimental Setup and Method</i>	23
<i>4. Results and Discussion</i>	25
<i>4.1. Gases under investigation</i>	25
<i>4.2 TDLAS Results</i>	26
<i>4.3 TDLPAS Results</i>	32
<i>4.4 Hybrid TDLAS-TDLPAS Results</i>	34
<i>4.5 Data Processing</i>	35
<i>4.6 Discussion</i>	46
<i>5. Conclusions</i>	49
<i>References</i>	49

Acknowledgements

I would like to thank a number of people that contributed so that this thesis was completed. First of all, I would like to express my appreciation to the members of the scientific committee, Prof. Dimitris Papazoglou (Associate Professor, Department of Materials Science and Technology, University of Crete), Dr. Petros Samartzis (Principal Researcher, IESL, FORTH) and especially Dr. Michalis Velegrakis (Research Director, IESL, FORTH), who has been the person conceiving the idea for this work and also guiding me throughout the whole period until this thesis was completed.

Furthermore, I would like to attribute special thanks to Dr. Panagiotis Siozos and Mr. Giannis Psyllakis, whose guidance, assistance and advice were of great importance for the completion of the thesis. Their scientific expertise was essential for the comprehension of all steps of the experimental procedure as well as of the theoretical background needed, while their experience helped in the solution of any problems encountered. I could not exclude from my acknowledgements Dr. Aggelos Philippidis for his constant support, advice and encouragement.

Last but not least, I would like to thank all the members of the Photonics for Agrofood and Environment Laboratory for their exceptional partnership and excellent cooperation.

Abstract

- ❖ EN/ Detection of toxic, explosive, hazardous gases and greenhouse gases (GHG) is of great importance. Several gas-sensing devices and sensors are currently available based on various methods however, there is a strong demand for improved sensitivity, reliability and simplicity. Laser-based infrared spectroscopy is a novel method increasingly applied for gas detection, thanks to its high selectivity, responsivity and sensitivity.

In the current work, two types of laser-based near-infrared spectroscopy techniques were employed for gas detection; Tunable Diode Laser Absorption Spectroscopy (TDLAS) and Tunable Diode Laser Photoacoustic Spectroscopy (TDLPAS). An experimental apparatus was developed for measurements of both spectroscopic techniques. The absorption spectra of five gases, carbon dioxide (CO_2), methane (CH_4), ammonia (NH_3), nitrous oxide (N_2O) and acetylene (C_2H_2) were recorded. A processing method of the acquired spectra was implemented and the limits of detection, in the present case, for each gas were estimated. Finally, a comparison of the two techniques was performed and a further discussion about their efficiency, usability and improvement of them is presented.

- ❖ ΕΛ/ Η ανίχνευση τοξικών, εκρηκτικών, επικίνδυνων αερίων και αερίων του θερμοκηπίου (GHG) είναι ένα διαχρονικό θέμα μείζονος σημασίας. Επί του παρόντος διατίθενται αρκετές συσκευές και αισθητήρες ανίχνευσης αερίων έχοντας ως βάση διάφορες μεθόδους, ωστόσο, υπάρχει μεγάλη απαίτηση για βελτιωμένη ευαισθησία, αξιοπιστία και απλότητα. Η φασματοσκοπία υπέρυθρου που βασίζεται σε λέιζερ είναι μια νέα μέθοδος που εφαρμόζεται όλο και περισσότερο για την ανίχνευση αερίων, χάρη στην υψηλή επιλεκτικότητα, απόκριση και ευαισθησία της.

Στην τρέχουσα εργασία, δύο τύποι τεχνικών φασματοσκοπίας λέιζερ στην περιοχή του εγγύς υπέρυθρου χρησιμοποιήθηκαν για την ανίχνευση αερίων, η φασματοσκοπία απορρόφησης λέιζερ με δυνατότητα συντονισμού (TDLAS) και φωτοακουστική φασματοσκοπία λέιζερ με δυνατότητα συντονισμού (TDLPAS). Κατά την διάρκεια της εργασίας, αναπτύχθηκε μια πειραματική συσκευή για μετρήσεις και των δύο φασματοσκοπικών τεχνικών. Καταγράφηκαν τα φάσματα απορρόφησης πέντε αερίων, διοξειδίου του άνθρακα (CO_2), μεθανίου (CH_4), αμμωνίας (NH_3), υποξειδίου του αζώτου (N_2O) και ακετυλενίου (C_2H_2). Έπειτα, εφαρμόστηκε μια μέθοδος επεξεργασίας των φασμάτων που αποκτήθηκαν και εκτιμήθηκαν τα όρια ανίχνευσης, στην παρούσα περίπτωση, για κάθε αέριο. Τέλος, έγινε σύγκριση των δύο τεχνικών καθώς και μια περαιτέρω συζήτηση για την αποτελεσματικότητά τους, τη χρηστικότητα και τη βελτίωσή τους.

1.Introduction

Gas detection and monitoring have been of great concern over the years for the scientific community as well as industry and agriculture. From toxic, explosive, hazardous gases to greenhouse effect gases (GHG), it is of great importance that reliable and effective sensors are developed for trace gas detection, assessing quality and safety of the product or environment. For this, numerous gas-sensing devices are currently available based on various methods. Laser-based infrared spectroscopy is one of the most widely used methods, thanks to its high selectivity, responsivity and sensitivity. A significant number of publications through years reveals the robustness, reliability and effectiveness of infrared spectroscopy in the field of trace gas detection.

Sumizawa et al. reported a detection limit of ≈ 50 ppbv (part per billion by volume) for nitric oxide, when monitoring it in diesel exhaust gas by cavity ring-down spectroscopy (CRDS) in the mid-infrared[1]. *Palduš et al.* recorded a 10 ppbv detection limit of ammonia, with CRDS by using continuous-wave quantum-cascade distributed feedback laser at 8.5 μm [2]. Cavity-ring down spectroscopy was employed by *Todd et al.* to trace explosives vapors in the mid-infrared (6–8 μm), recording detection limits as low as 75 ppt for trinitrotoluene (TNT), with similar concentration levels for other explosives as well[3]. A detection limit of 1.94 ppmv (part per million by volume) for CO_2 was reported from *Xin et al.* with an open-path measuring system based on tunable diode laser absorption spectroscopy (TDLAS)[4]. *Zheng et al.* reported detection limits as low as 28 ppb for nitric oxide from cigarette burning, using a TDLAS set-up with quantum-cascade laser at 5.24 μm [5]. *Ciu et al.* recorded minimum detection limits of 100, 40, and 50 ppm for CH_4 , C_2H_2 , and C_2H_4 respectively employing TDLAS with DFB-type lasers in the near-infrared region[6]. Carbon dioxide detection using NIR diode laser with photoacoustic spectroscopy was reported by *Li et al.*, recording a detection limit of 30 ppmv[7]. DFB diode laser photoacoustic spectroscopy was applied for trace gas analysis by *Alahmari et al.*, reporting detection limits of 160 ppmv and 22 ppmv for CO_2 and H_2S respectively[8]. Ethylene and ammonia were detected down to concentrations of 16 ppbV and 42 ppbV respectively with the use of a continuous wave CO_2 infrared laser employing photoacoustic spectroscopy, *Lima et al.* reported[9].

In this work, two types of laser-based near-infrared spectroscopy techniques were employed for gas detection, *Tunable Diode Laser Absorption Spectroscopy* (TDLAS) and *Tunable Diode Laser Photoacoustic Spectroscopy* (TDLPAS). A lab-assembled array was developed for measurements of both spectroscopic techniques making use of DFB-type (Distributed Feedback) lasers as the emitting source. In general, DFB lasers are available for emission in different spectral regions at least in the range from 0.8 μm to 2.8 μm and typical output powers are some tens of milliwatts. Five gas species were investigated, including carbon dioxide (CO_2), methane (CH_4), ammonia (NH_3), nitrous oxide (N_2O) and acetylene (C_2H_2). *Carbon dioxide* is the primary greenhouse gas emitted. It is naturally present in the atmosphere as part of the Earth's carbon cycle (the natural circulation of carbon among the atmosphere, oceans, soil, plants, and animals). While CO_2 emissions come from a variety of natural sources, human-related emissions

are responsible for the increase that has occurred in the atmosphere the past years. With the increasing use of fossil fuel combustion and emissions from industry and automobile exhaust, the CO_2 concentration in the atmosphere has increased dramatically, “fueling” the greenhouse effect, which has led to global warming, glacier melting, and a rise in sea levels. *Nitrous oxide* is a minor component of the atmosphere with great interest for environmental studies. Its concentration is about 300 ppb and “human disruption of the nitrogen cycle is probably responsible for the steeply increasing levels of N_2O in recent years”. It contributes to the destruction of stratospheric ozone, to the greenhouse effect and has direct impact on human health, all features providing further motivations to the present investigation. *Ammonia* is an important species for the refrigeration and fertilizer products. Though, its widespread use and toxic nature introduce a need to monitor its presence so that pollution can be minimized, as it poses serious health risks. It is released to the atmosphere as a major agriculture emission, mainly through the rapid hydrolysis of urea excreted by livestock. *Methane* is one of the most abundant gases on earth, main constituent of natural gas and greenhouse effect. As far as the latter is concerned, human emissions from livestock, agriculture and industry along with natural emissions from wetlands, rank methane among first contributors to the effect. It is significant that measurements for monitoring ongoing emission changes of methane are made, providing incentive for this present work. *Acetylene* is one of the most important hydrocarbons species used worldwide for a number of purposes. From portable lighting to plastics production and from metals heat treatment to synthesis of several inorganic and organic compounds, ranks among first species of nowadays importance. It originates predominantly from anthropogenic activity including automotive industry and biomass burning. Absorbing gases’ spectra enabling both techniques are presented and a calculation of LLD (Lower Limit of Detection) achieved, along with a comparison between two applied spectroscopic methods, are discussed.

2.Theory

2.1. Near-Infrared Spectroscopy

NIR spectroscopy is a significant and widely used analytical technique among spectroscopists. NIR spectroscopy is considered as vibrational spectroscopy since it operates at vibrational energy levels. An interpretation of NIR spectra results in extracting valuable information about the vibrational “profile” of a molecule. For the purpose of comprehending the origins of NIR spectroscopy, it is necessary to know about its basics. At ambient temperatures, atoms forming chemical bonds displace each other. When energy is given to the molecule in the form of *radiation*, the amplitude of their vibrations increases. In other words, interaction of a molecule with radiation results in the absorption or emission of a quantum of energy. This energy is given by the famous Planck’s equation which follows[10]:

$$E = h\nu \quad (1)$$

where h is Planck’s constant (equal to 6.6×10^{-34} J s) and ν is the frequency. Radiation can be considered as mutually perpendicular magnetic and electric fields oscillating in single planes at right angles to each other. Where in phase, these fields propagate as a *sine* wave and the aforementioned frequency ν is the number of wave cycles per second. NIR spectroscopy is defined in the region between 780 and 2500 nm, where light is absorbed, elevating the molecule to certain excited vibrational states. This leads to the observed absorption bands associated with overtones and combinations of fundamental vibrations. Certain physical models describe these molecular vibrations.

2.1.1 Harmonic Oscillator

For a vibrating system, the simplest model that describes the interaction of matter and radiation can be presented via a harmonic oscillator in which, two spherical masses (m_1 and m_2) are connected by a spring with a given force constant (k) that leads to changes in the internuclear distance. The vibration frequency ν (based on a combination of Newton’s force law with Hook’s law) can be calculated by the following equation[10]:

$$\nu = \frac{1}{2\pi} \sqrt{\frac{k}{\mu}} \quad (2)$$

where μ is the reduced mass of the bonded atoms, such that $\mu = m_1 m_2 / (m_1 + m_2)$. According to this formula, the frequency of the vibration provides information on the

chemical structure of the compound under examination. It depends on the atoms involved in the chemical bond and this is the basis of infrared spectroscopy. Due to the fact that the molecular vibration is described by a simple harmonic oscillator, the potential energy V is a function of the displacement of the vibrating atoms[10]:

$$V = \frac{1}{2}k(d - d_e)^2 = \frac{1}{2}kx^2 \quad (3)$$

where d is the internuclear distance, d_e is the internuclear distance at equilibrium, and x is the displacement of vibrating atoms. The potential energy is a parabolic function, symmetrical about the equilibrium bond length d_e as presented in Figure 2.1, which shows the potential energy as a function of atomic displacement from the equilibrium position. The figure also shows the effect of photon absorption on the energy and amplitude of vibration.

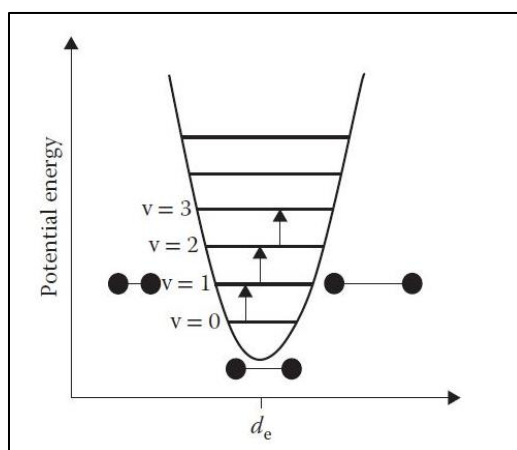


FIGURE 2.1: Schematic representation of the harmonic model for the potential energy of a diatomic molecule. (d_e = equilibrium distance)(adapted from [10])

A comprehension of the concept of vibrational energy is provided through this harmonic oscillator, but still this model cannot be used for molecules because molecular systems do not follow the continuous energy profile that the classical model describes. Based on quantum mechanics, Schrödinger proposed an equation in which he showed that the harmonic oscillator might have only certain discrete values called energy levels[10]:

$$E_{vib} = hv \left(u + \frac{1}{2} \right) \quad (4)$$

where u is vibrational quantum number (0, 1, 2, ...).

The vibrational energy levels $G(u)$ are expressed in wavenumber units (cm^{-1}) as follows[10]:

$$G(u) = \frac{E_{vib}}{hc} = \bar{\nu} \left(u + \frac{1}{2} \right) \quad (5)$$

where $\bar{\nu}$ is the wavenumber of the vibrational transition. As shown in Figure 2.1, the energy levels are equally spaced. In the harmonic oscillator, the only transitions allowed are those between neighboring and equidistant energy levels. At room temperature, most of molecules reside at the ground vibrational level $u = 0$. Consequently, the first transition allowed is the one to energy level $u = 1$, called the “*fundamental transition*”. The other transitions originate from vibrationally excited levels, namely *hot bands*. The allowed transitions follow some selection rules that can be deduced via the transition moment given by the following formula[10]:

$$P_{u'' \rightarrow u'} = \int \psi_{u'}^* \varepsilon \psi_{u''} d\tau \quad (6)$$

where $\psi_{u'}$ and $\psi_{u''}$ are the wave functions of the states u' and u'' , while $*$ indicates the complex conjugate of u' .

On the other hand, ε is the dipole moment. Its expression is a linear function of x about the equilibrium nuclear distance[10]:

$$\varepsilon = \varepsilon_0 + \left(\frac{d\varepsilon}{dx} \right) x \quad (7)$$

where ε_0 is the dipole moment at the equilibrium point. By substituting the appropriate wave functions and dipole moment from Equation (7) into Equation (6), the transition moment for the $u'' \rightarrow u'$ transition can be calculated. It suggests that transitions are allowed for a transition moment other than zero. This is able to happen only if the vibration is accompanied by a dipole moment change, meaning that only heteronuclear diatomic molecules exhibit transitions between photons and then molecule vibrations. Because the vibrational quantum number can change by only one unit, transitions occur only if [10]:

$$\Delta u = \pm 1$$

Taking into account the Boltzmann distribution, at room temperature, most molecules are at the ground energy vibrational level $u = 0$ and therefore the allowed fundamental transition is from $u = 0$ to $u = 1$. Further allowed transitions originate from each excited vibrational level: $u = 1$ to $u = 2$, $u = 2$ to $u = 3$ and so on. Because these levels have a relatively low population, hence the corresponding bands are lower than fundamental ones. The harmonic oscillator model implies, nevertheless, that transitions from the first, second, or third excited level have the same frequency (energy) as that of the fundamental transition. This model is disappointing in terms of the fundamentals of NIR spectroscopy, because it does not allow transitions where the difference between two vibrational states Δu is greater than 1. Transitions observed in the NIR region where $\Delta u = 2$ or greater, are forbidden and overtone bands should not exist. Additionally,

harmonic model imposes restrictions that make vibrations independent and their combinations would not exist, whereas combination bands are observed in NIR spectra.

2.1.2 Anharmonic Oscillator

Along with the issues encountered in the model of harmonic oscillator mentioned above, this model indicates that the molecule can store infinite energies without bond breaking.

A variable behavior of the bond force, though, is observed when the atoms move, and molecules dissociate when enough energy is applied in extending the vibrating bond (bond dissociation—anharmonicity). When the atomic nuclei approach (Coulombic repulsion) each other, repulsion is observed between electronic clouds. Figure 2.2 shows a more realistic mechanical model for a diatomic molecule that focuses on the *nonideal* behavior of the harmonic oscillator.

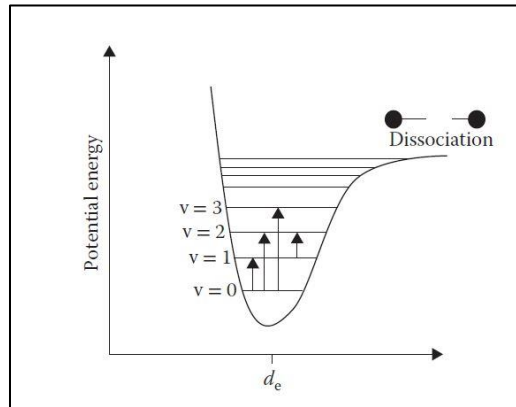


FIGURE 2.2: Schematic representation of the anharmonic model for the potential energy of a diatomic molecule. (d_e = equilibrium distance)(adapted from [10])

A complex function describes the potential energy as a quadratic function of the displacement extended by adding higher order terms of displacement[10]:

$$V = \frac{1}{2}kx^2 + \frac{1}{2}k_ax^3 + k_bx^3 + \dots \quad (8)$$

with $k_a, k_b \ll k$.

This expression is used in the Schrödinger equation to estimate the vibrational energy of allowed states of the anharmonic oscillator[10]:

$$E_{vib} = hv \left(u + \frac{1}{2} \right) - y \left(u + \frac{1}{2} \right)^2 \quad (9)$$

where y is the anharmonicity constant.

Some restrictions are also imposed from the anharmonic model on the possible energy states of the molecules, but it allows transitions with $\Delta u = 2$ or higher and the existence

of combination bands between vibrations. Furthermore, the vibrational energy levels are not any longer equidistant and the separation between two adjacent energy levels decreases with v , the vibrational quantum number. Instead of the parabolic shape, the potential energy curve is represented by an asymmetric Morse function, as shown in Figure 2.

The vibrational energy levels $G(u)$ are expressed in wavenumber units (cm^{-1}) as follows[10]:

$$G(u) = \frac{E_{vib}}{hc} = \bar{\nu} \left(u + \frac{1}{2} \right) - x_e \bar{\nu} \left(u + \frac{1}{2} \right)^2 \quad (10)$$

where x_e is the anharmonicity constant.

Comparing to Equation (5), we must mention that unlike the harmonic oscillator, the energy levels are no longer equally spaced. In order for NIR spectral vibrations to occur, apart from the change in the dipole moment, a large mechanical anharmonicity is also necessary. As far as the anharmonic model is concerned, the dipole moment has a non-linear dependence with the interatomic distance, as presented in the following expression[10]:

$$\varepsilon = \varepsilon_0 + \left(\frac{d}{dx} \right) x + \frac{1}{2} \left(\frac{d^2 \varepsilon}{dx^2} \right) x^2 + \dots \quad (11)$$

This kind of anharmonicity could *allow* the occurrence of overtones and combination bands. This corresponds to transitions between energy levels that differ by two or three quantum number units ($\Delta u = +2, +3, \dots$). It is obvious that anharmonicity is the basis of NIR spectroscopy. It defines the frequency and intensity of overtone absorption bands.

2.1.3 NIR Spectra

Theory of NIR spectroscopy makes possible for one to comprehend the origin of vibration bands of NIR spectra. When the displacement of the atoms in a vibration yields a change in the dipole moment of the molecule and the energy of radiation matches to the energy difference between two vibrational levels, vibrations occur.

An absorption spectrum, composed of several bands is generated from specific energies absorbed, within a certain energy amount that corresponds to a definite wavelength range. Some frequencies are absorbed and others are not. This phenomenon is presented on a graph showing the absorption intensity versus wavelength (λ) or wavenumber ($\bar{\nu}$) or energy (eV). Intensity of absorption bands depends on the magnitude of the dipole change during the displacement of atoms in a vibration and on the degree of anharmonicity. Bonds exhibiting a low constant of anharmonicity have much lower overtone intensities.

Absorption bands with different intensities in the NIR spectrum are a result of energy absorption by specific functional groups in a sample. The most significant bands present in the NIR region are related to overtone and combination bands of the fundamental molecular vibrations of the O–H, N–H, C–H and S–H functional groups observed in the midinfrared region. NIR bands very often overlap. Since hydrogen atom is the lightest atom, bonds with hydrogen exhibit the largest vibrations [$x_e(u \text{ C-H}) \sim 1.9 \times 10^{-2}$]. These bonds also have high bond energy and high anharmonicity compared with fundamental vibrations in the MIR region. Carbonyl stretching bands are less anharmonic [$x_e(u \text{ C=O}) \sim 6.5 \times 10^{-3}$], with their higher overtones presenting low intensity. Hence, we may predict that overtones and combinations of the fundamental vibrations of these bonds occur in the NIR region, but they are of much weaker intensities than those observed for fundamentals.

Resonance observed in the NIR spectra is also a phenomenon worth noting, which contributes to spectra being complicated by the presence of two bands, rather of one, in the combination spectral region. Resonance occurs between an overtone and a fundamental band when their energy difference is very low (Fermi resonance), leading to a higher separation of the two band positions and also in the intensity of the overtone band, or, additionally, this can occur as a result of the interaction between a combination band and two high-level overtones of a molecule (Darling–Dennison resonance). Considering all of the above, one can easily suggest that NIR spectra are dominated by overtone and combination absorption bands related to molecules containing hydrogen bonds, such as -CH and -OH. Generally, the bands at smaller wavenumbers (longer wavelengths) present greater magnitude of intensity and are far better resolved than their corresponding higher overtones at larger wavenumbers (shorter wavelengths).

2.1.4 Number of vibrational modes

In order to calculate the vibrational motions of a molecule, *degrees of vibrational modes* for *linear* and *non-linear* molecules must be taken under consideration. These vibrational modes derive from the degree of freedom of a molecule, which is the number of variables required to describe the motion of a particle completely. The degrees of vibrational modes for **linear molecules** can be calculated using the formula:

$$3N-5$$

Degrees of freedom for **nonlinear molecules** can be calculated using the formula:

$$3N-6$$

2.2 Tunable Diode Laser Absorption Spectroscopy (TDLAS)

Absorption spectroscopy using diode lasers has been used for measuring gas temperatures and concentrations for at least 25 years. TDLAS, employs a tunable diode laser (TDL) with a very narrow linewidth to obtain gas absorption lines at very high

spectral resolution by current or thermal tuning of the emission wavelength. Recently, with increasing maturity and broader availability of laser light sources and peripheral electro-optical components, TDLAS has found extended industrial use. By this technique, multiple gas flow properties such as *species concentrations*, *temperature*, *pressure* and *velocity* can be measured[11].

In the case of *infrared* region of electromagnetic spectrum, many important gases show absorption in this particular spectral region. In Figure 2.3 corresponding absorption bands in the *near infrared (NIR)* and *mid infrared (MIR)* for certain gases are presented. The absorption lines in gases are narrow. This phenomenon can be exploited for probing individually isolated peaks by using a highly monochromatic light source. The NIR absorption spectra contain a multiplicity of lines of several overtone and combination bands, as aforementioned in section 2.1.3. For example, there are over 50,000 transitions at 1000 K for H₂O between 1 and 2 μm ! These transitions are tabulated in specific spectral databases such as HITRAN (hitran.iao.ru/) or GEISA (geisa.aeris-data.fr/)[11].

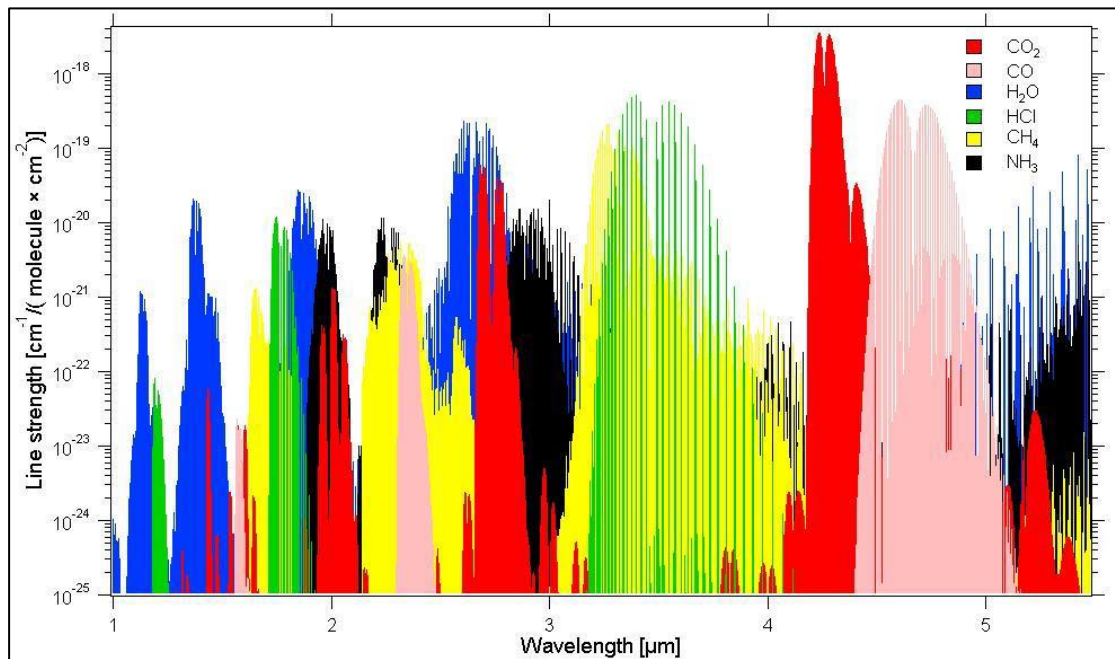


Fig. 2.3: Absorption lines of CO₂, CO, H₂O, HCl, CH₄ and NH₃ in the infrared (adapted from [11]).

As far as laser sources are concerned, those in the MIR spectral region are rather difficult to operate, since they mostly require cryogenic (liquid nitrogen) cooling for *cw* (continuous wave) operation. Cost is another deterring factor for MIR laser sources as they are much more expensive than NIR ones. Therefore, room-temperature operated diode lasers in the NIR spectral region are much more widely used[11]. Weak transitions though need a higher measurement sensitivity of the sensor. By looking up the position of absorption lines in spectral databases (HITRAN/GEISA), absorption lines that are isolated can be selected for measurements with no interference.

Nevertheless, although an absorption line is isolated and separated from absorption lines of other gas compounds that may be present, it is not truly unaffected by these other gases in the measurement volume due to the fact of influences on the absorption line shape (broadening effect).

Regarding small molecules, the absorption bands are composed of individual lines, which can be probed by spectroscopic techniques. In general, compounds with more than four atoms have complex vibrational NIR spectra where the assignment of individual spectral lines is far from possible, except under certain experimental conditions.

In tunable diode laser absorption spectroscopy, individual absorption lines, as depicted in Figure 2.3, are probed. Therefore, a diode laser with an emission frequency (wavelength) proper to match to a suitable absorption line is selected. The experimental setup essentially consists of the laser and the detector with a sample volume in between. A simple setup of TDLAS is depicted in Fig. 2.4. I_0 is the initial light intensity (the so-called *baseline*), and I is the penetrated light intensity (signal containing the absorption information).

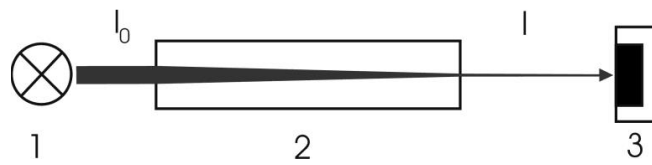


Fig. 2.4: Experimental setup for TDLAS. 1: Monochromatic light source; 2: sample volume; 3: detector; I_0 is the initial light intensity and I the transmitted light intensity.

The fundamental theory lying behind absorption spectroscopy is the *Beer-Lambert law*, which describes the relationship between the transmitted intensity I and the initial intensity I_0 through the sample. Its expression is presented in Equation (12) with multiple forms[12]:

$$\begin{aligned} I(\nu) &= I_0(\nu) \exp(-\alpha_\nu) \\ &= I_0(\nu) \exp(-k_\nu L) \\ &= I_0(\nu) \exp(-n\sigma_\nu L) \end{aligned} \tag{12}$$

where α_ν is the spectral absorbance, k_ν [cm^{-1}] is the spectral absorption coefficient, L [cm] is the absorption pathlength, n [molecule/ cm^3] is the number density of the absorbing species and σ_ν [$\text{cm}^2/\text{molecule}$] is the absorption cross-section. The subscript ν denotes the spectral dependence of the parameter on the light frequency ν . The spectral absorbance is linked to the spectral absorption coefficient k_ν : $\alpha_\nu = k_\nu L$. The absorption coefficient is related to the cross section σ_ν of the molecules by: $k_\nu = n\sigma_\nu$. It is clear from above equations that, when knowing the absorption cross-section σ_ν , one can obtain the number density of the absorbing species, hence the concentration of the analyzed gas in a closed volume.

2.3 Tunable Diode Laser Photoacoustic spectroscopy(TDLPAS)

2.3.1 The Photoacoustic Effect

The photoacoustic effect is the formation of acoustic waves after the absorption of light by a material and was firstly reported by Alexander Graham Bell back in the 1880's. Bell accidentally discovered the effect while experimenting with his "photophone". That is, sunlight was focused onto a sample contained in a selenium cell that was connected to a listening tube. When the sunlight was repeatedly blocked and unblocked, sound could be heard through the listening tube at the sunlight chopping frequency[13]. Although discovered in 1880's, photoacoustic effect laid completely dormant for nearly 50 years, until the advent of the microphone and it was not before late 1960's that an upsurge in its use began due to the availability of laser sources[13], [14]. Photoacoustic spectroscopy relies on the photoacoustic effect for the detection of absorbing analytes. Main difference from conventional optical techniques lies mainly in that even though the incident light is in the form of photons, the interaction of these photons with the material under investigation is studied not through subsequent detection and analysis of photons after interaction (transmitted, reflected or scattered), but, instead, through a direct measurement of the effects of the energy absorbed by the material[15].

2.3.2 Nonradiative transitions and photoacoustic signal generation

In order to comprehend the photoacoustic effect, it is necessary to know more about its basics. Light absorbed by a molecule will excite a fraction of the ground-state molecular population into higher energy levels (rotational, vibrational, electronic). These excited states will subsequently relax through *radiative* (i.e., fluorescence, phosphorescence) or *nonradiative* (i.e., intersystem crossing, internal conversion) pathways or a combination thereof (Fig 2.5). The nonradiative transitions will channel at least part of the absorbed energy into *heat* in the localized region of the excitation light beam. In a gas this energy appears as kinetic energy of the gas molecules, while in a solid appears as vibrational energy of ions of atoms (phonons)[16], [17]. If, now, the incident light beam is intensity modulated, then this optical modulation results in a coherent modulation in the temperature of the sample. Consequently, this further leads to a periodic pressure fluctuation with a modulation frequency equal to the optical modulation frequency. This pressure fluctuation is, of course, the *photoacoustic signal*, which in fact is a sound wave, readily detectable by a sensor[13].

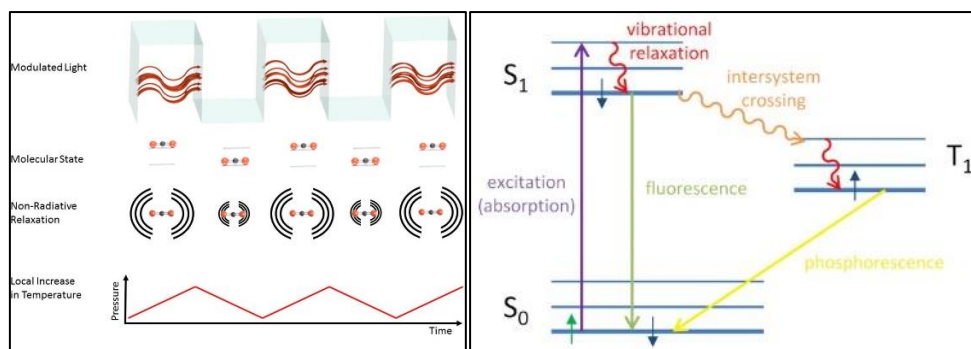


Fig 2.5: i) Simplified schematic depiction of the most relevant processes for photoacoustic signal generation. Intensity modulation of radiation excites molecular states. Due to non-radiative relaxation processes, part of the photon energy is converted into heat, leading to a local increase in temperature and pressure. Periodic light modulation thus leads to a pressure wave that may be detected using suitable detectors (adapted from [17])

ii) Excitation and de-excitation processes. For de-excitation processes, fluorescence and phosphorescence include radiation emission while vibration relaxation (or internal conversion) and intersystem crossing are radiationless processes (adapted from [18])

2.3.3 Relaxation processes and heat release

Upon radiation, excitation of vibrational levels leads to a complete transformation of the absorbed energy into heat, whereas for electronic excitation competing pathways exist such as emission of radiation and photoinduced reactions[15], [19] (Fig 2.6).

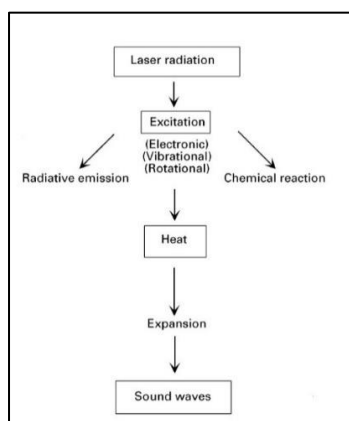


Fig 2.6: Processes occurring during photoacoustic signal generation. The absorbed photon energy is partly transformed into heat (adapted from [15])

In the case of vibrational excitation of gas molecules, radiative emission and photochemical reactions do not play an important role, because the radiative lifetime of vibrational levels is long compared to the time needed for collisional deactivation (responsible for heat release) at ordinary pressures and the absorbed energy is too small to induce reactions[15], [16]. However, in the case of electronic excitation, the emission of radiation and chemical reaction processes may compete efficiently with collisional deactivation. Chemical reactions may also contribute to the release of heat, and thus

they may increase the photoacoustic effect. If photodissociation occurs, for instance, the local increase of the number of molecules generates a local pressure and, hence, a temperature rise[15]. The latter type of excitation is not studied in the current work.

2.3.4 Photoacoustic signal generation in gases – The governing equations

Photoacoustic signal generation is generally described in two steps. The first one concerns the *heat production* in the gas sample and the second one the *generation of acoustic waves*[16]. For the first step, heat production in a gaseous sample excited by an intensity modulated light beam (laser) may be described by the use of molecule population levels. In the simple case of a two-level system, where the absorbing gas contains a molecule density N , the vibrational ground state (E_0) can be expressed by a density $(N-N')$ and the excited state (E_1) with a density N' [20](Fig 2.7).

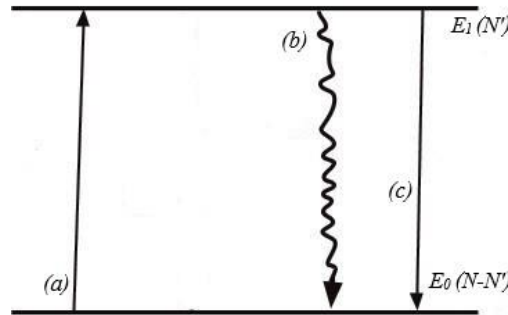


Fig 2.7: Two-level molecular model showing the radiative and nonradiative transitions between energy states E_0 and E_1 . (a) Absorption of incident light, (b) Nonradiative de-excitation, (c) Radiative de-excitation (adapted from [20])

Heat is generated in the gas by the non-radiative decay of the excited state population N' . The rate of heat generation is given by[16]:

$$H = N' \frac{h\Delta\nu}{\tau_n} \quad (13)$$

where $h\Delta\nu$ is the average thermal energy released due to the nonradiative de-excitation of the excited state and (τ_n) is the lifetime of a nonradiative relaxation. The inverse time τ^{-1} refers to the sum of reciprocal lifetimes of nonradiative (τ_n) and radiative (τ_r) relaxation[16]:

$$\tau^{-1} = \tau_n^{-1} + \tau_r^{-1} \quad (14)$$

For typical atmospheric conditions, τ_n is on the order of 10^{-6} - 10^{-9} s, while τ_r is between 10^{-1} - 10^{-3} s. In consequence, the spontaneous emission of the vibrational levels is long

compared to the time needed for a collisional deactivation, as mentioned already in ***Relaxation processes and heat release***, and hence τ can be approximated by τ_n . Thus, the whole absorbed energy in the sample is generally released as heat. If the de-excitation process results in the conversion of the excited state to the ground state, as assumed with the two-level system, then $\Delta v \approx v_{\text{laser}}$.

Taking into account that $\tau_n \approx \tau$, the heat production rate can be expressed as[16]:

$$H = N' \frac{h\nu_{\text{laser}}}{\tau} \quad (15)$$

For low modulation frequencies $\omega \ll 10^6$, $\omega\tau \ll 1$, the heat production rate is simplified to obtain[14], [16]:

$$H(\mathbf{r}, t) = aI(\mathbf{r}, t) \quad (16)$$

where \mathbf{r} describes the position and t is the time, a [cm^{-1}] is the absorption coefficient (mentioned also in section ***Tunable Diode Laser Absorption Spectroscopy (TDLAS)*** as k_v) of the gas sample and $I(\mathbf{r}, t)$ is the incident light intensity. The condition $\omega\tau \ll 1$ is usually satisfied since the modulation frequencies are in the kHz range or near.

For the second step, sound and thermal waves can be described by classical disciplines of physics such as fluid mechanics and thermodynamics. The physical laws governing the system are the equations of *Navier-Stokes*, of *thermal diffusion*, of *mass-density continuity* and a *thermodynamic state equation*. The physical quantities characterizing the acoustic and thermal processes are the temperature T , pressure P , density ρ and the three components of the particle velocity vector \mathbf{u} . This complex problem cannot be solved for a general case and some simplifications must be included. Thus, by eliminating the variables T , ρ , and \mathbf{u} (and by neglecting the influence of the thermal and viscous interactions of the gas), a linearized (inhomogeneous) wave equation can be derived for the acoustic pressure changes, p [13], [14], [16]:

$$\nabla^2 p(\mathbf{r}, t) - \frac{1}{c_s^2} \frac{\partial^2 p(\mathbf{r}, t)}{\partial t^2} = - \frac{(\gamma - 1)}{c_s^2} \frac{\partial H(\mathbf{r}, t)}{\partial t} \quad (17)$$

where c_s is the velocity of sound, $\gamma = C_p/C_v$ is the ratio of the specific heat capacity at constant pressure C_p to the specific heat capacity at constant volume C_v , \mathbf{r} describes the position and t is the time. Since the transformation of the absorbed light into heat is usually modeled by a relaxation process, as mentioned above, the wave equation (17) is applied to calculate the sound-pressure field and relate pressure changes with the heat production. It is clear that if the heat input is constant, the term $H(\mathbf{r}, t)$ equals zero and no pressure wave is generated. Thus, the heat input must be modulated, which requires that the incident radiation be also amplitude or frequency modulated. In that manner, a modulated laser beam generates periodic sound due to the periodic localized heating of the gas[14].

3. Materials, Methods and Instrumentation

Experimental Setups

Gas measurements were conducted in three consecutive steps, concerning the optical methods involved. Firstly, TDLAS was employed to extract the results for absorbing species, operating the experimental setup for this spectroscopy in specific conditions. Then PAS followed, as soon as the development for the experimental setup was completed. Lastly, measurements for both optical methods were made in a hybrid TDLAS-PAS experimental array, enabling us to compare the efficiency of each method in the same specific conditions. Every component of setups was manually attached, adjusted or modified in the lab so as to fit in the array and make possible for measurements to happen.

3.1 TDLAS Experimental Setup and Method

The schematic of Fig. 3.1 depicts the TDLAS experimental setup. Components are discussed below in detail as well as the measuring process.

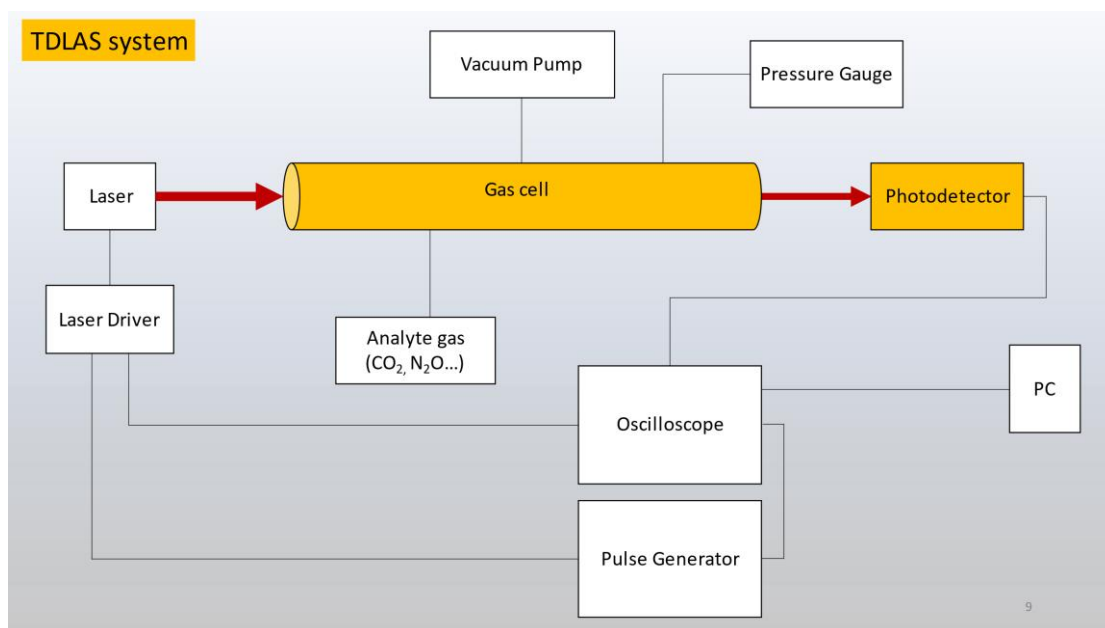


Fig. 3.1: Schematic diagram of TDLAS experimental setup

The **laser sources** used in the current work were four continuous wave (cw), DFB-type diode lasers, operating on a single frequency each. A collimator of 1.2 mm diameter was used to align the laser beam. The two first, operating at a central wavelength of 1521 nm (6574 cm^{-1}) (EP1521-0-DM-B01-FA, Eblana, Ireland) and 1520 (6578 cm^{-1}) (EP1521-0-DM-B01-FA, Eblana, Ireland) respectively, with a linewidth of 2 MHz and maximum output power of 14 mW, are used for N₂O, NH₃ and C₂H₂ detection. The third has a central wavelength of 1572 nm (6361 cm^{-1}) with a linewidth of 1 MHz and

maximum output power of 60 mW (#LD-1550-0060-DFB-1, Toptica, Gräfelfing, Germany) and is used for the detection of CO₂. The fourth has a central wavelength of 1653.7 nm (6047 cm⁻¹) with a linewidth lower than 2 MHz and maximum output power of 15 mW (PL-DFB-1650-A-A81-PA, Id-pd, Singapore) for the detection of CH₄. These wavelengths were carefully selected so as to satisfy the conditions of matching to characteristic absorption lines of the analyzed species.

A DFB-*cw*-diode laser is a handy light source for spectroscopists because it is compact, room-temperature operated and offers bright, monochromatic light. Also, the lasers can be tuned in their emission wavelength[11]. This wavelength-tuning or wavelength-scanning is done by altering temperature or injection current of the laser with the use of a **laser driver**. Each laser is controlled by a current and temperature driver (SF8075-ZIF14, Maiman, Saint-Petersburg, Russia). The laser *wavelength* λ [nm] is usually expressed as a *wavenumber* $\bar{\nu}$ [cm⁻¹], as wavenumbers are frequently used by spectroscopists because they are directly proportional to the energy.

In detail, the laser scans over the entire area of absorption peaks in order to record the full spectral feature. Lasers can be wavelength-tuned in a narrow range by either varying the *temperature* [K] or the *drive current* [mA]. In this work, the drive current is set on a stable value, efficient for signal generation and the temperature is modulated via a **pulse generator** (DG822, Rigol, Suzhou, China). The pulse generator applies a varied voltage on the laser driver which leads to a temperature modulation. Temperature can be controlled thermoelectrically by a Peltier element. This modulation causes a continuous and repetitive change in the laser wavenumber.

Gas cell was manually assembled in the lab so that it contains the species to analyze. Glass windows (no absorption of NIR light) were placed in Brewster angle on the two edges of the cell, so as to avoid further reflections of laser beam. Gas for analysis was injected through a Teflon tube from a gas cylinder and the pressure inside the cell was measured with a Pirani pressure gauge. Gas cell provided a 1.4 m pathlength for the beam to react with the absorbing species.

Incident light, after having passed through the gas cell, was detected from a *Ge*-type **photodetector** (PDA50B2, THORLABS, Newton, NJ, USA). The photodetector has a detection range from 800 to 1800 nm, suiting perfectly to the wavelength range covered by all laser sources used.

TDLAS measurements were made in *vacuum conditions* inside the cell. A **vacuum pump** was used so that air or a past measurement's content was removed to a certain degree ($\sim 10^{-3}$ mbar). Before injecting certain given quantities of the analyte, a *background* measurement of the incident light beam in vacuum was made, termed *baseline* (I_0). Then, injection of analyte followed and measurement was repeated, termed *signal* (I), being the one containing the desired information. A linearly rising ramp has proven convenient to apply to the laser as shown in Fig. 3.2 (a) (dotted line).

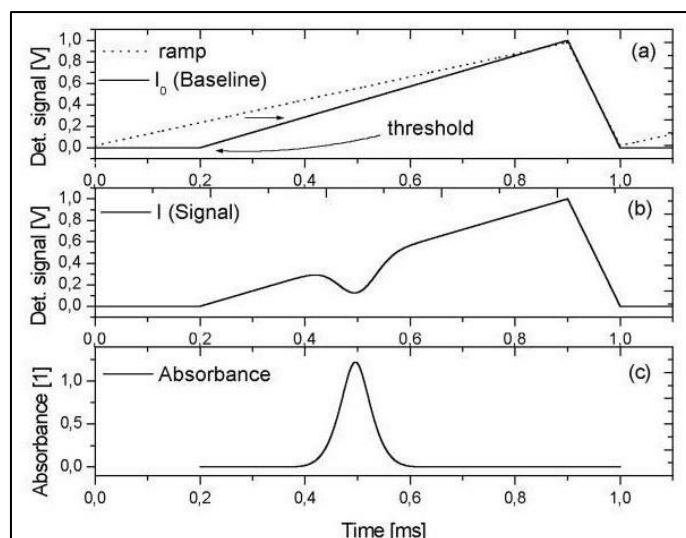


Fig. 3.2: Recording of an individual absorption line. (a) shows the current ramp applied to the laser and the baseline (I_0), (b) gives the transmitted signal (I). In (c), the absorbance a is shown (adapted from [11])

As soon as the threshold input voltage at the given current is reached, the device starts lasing. The initial light intensity (I_0), (*baseline*) in Fig. 3.2, then scales approximately linearly with input voltage. At the same time, the emission wavenumber shifts. As the input voltage increases (temperature decreases as is inversely proportional), the laser wavenumber increases. In Fig. 3.2 (b), an absorption peak can be seen as a dip on the transmitted light intensity (I), (signal), at the resonance wavenumber $\bar{\nu}$ (resonance wavelength λ). In Fig. 3.2 (c), the absorbance $a = \ln(I_0/I)$ has been plotted.

A digital *oscilloscope* (DSOX1204G, Keysight, Santa Rosa, CA, USA), connected to the photodetector, was employed for the visualization of signal and transportation of it to a personal computer. Data recorded in .csv format contained an average of 8 scans for every certain quantity of analyte examined as well as for the background. Origin 2018 was used for the data editing procedure. Further details and parameters of measurements are presented alongside in Results and Discussion section.

3.2 TDLPAS Experimental Setup and Method

The schematic of Figure 3.3 depicts the TDLPAS experimental setup. Components are discussed below in detail as well as the measuring process.

Since most of the components for the schematic above are the same that were utilized for TDLAS experimental setup, only new insertions or modifications of existed components will be discussed. Main difference between the two setups lies on the chopped laser beam, needed for the photoacoustic effect to emerge. Unlike TDLAS, where the laser was focused uninterrupted on the gas cell, in PAS, a *mechanical chopper* (360C-OEM, Scitec, Trowbridge, UK) modified the beam so that it reached the cell in cycles of a certain frequency. By the use of a *chopper driver*, a desired

frequency was adjusted to modify the incident laser beam. In order to reduce chopper-induced sound vibrations in air that can be transmitted to the microphone detector as noise-interference, a small housing with a small hole for the laser beam to enter and exit was built in 3D printer.

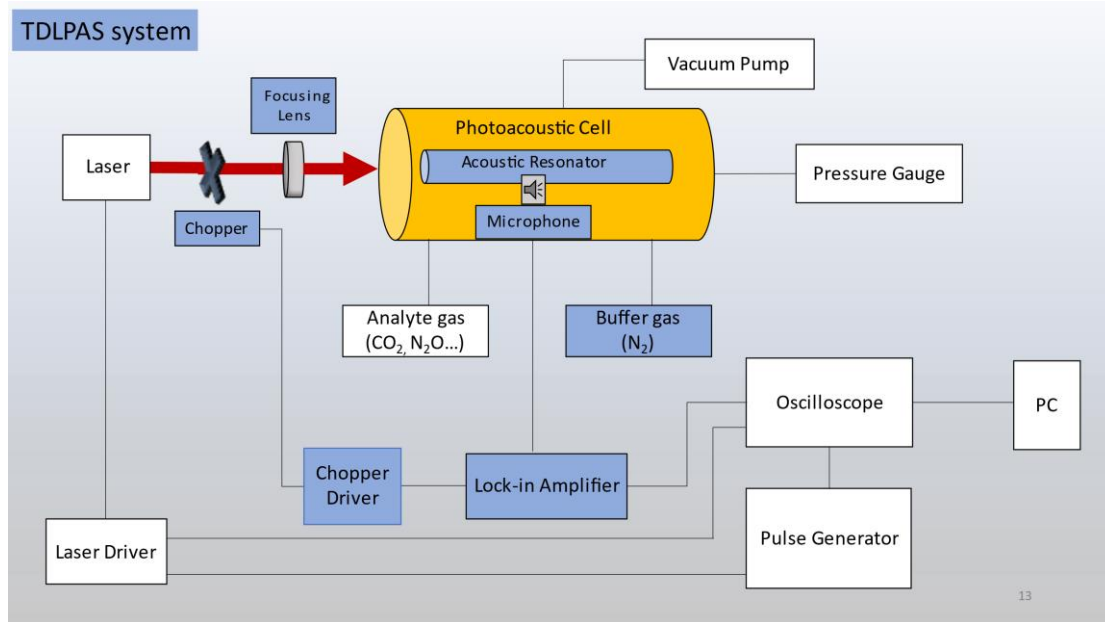


Fig. 3.3: Schematic diagram of TDLPAS experimental setup

The gas cell was properly modified to a *photoacoustic cell* by inserting an acoustic **resonator**. Acoustic resonator, an open-open end aluminum cavity in the current work, is a critical component for the photoacoustic signal so that the latter can be detected. More specifically, when the modulation frequency is equal to one of the eigenfrequencies of the cavity, the energy from many modulation cycles is accumulated in a standing acoustic wave and the system works as an acoustic amplifier. The final signal amplification is determined by the total losses of the resonator. After an initial transient state, during which energy is accumulated in a standing acoustic wave, a steady state is reached in which the energy lost per cycle due to various dissipation processes is equal to the energy gained per cycle due to the absorption of photons. The degree of amplification of a resonator is described by a quantity called *Q-factor*, given by [13], [16]:

$$Q = \frac{2\pi \text{ accumulated energy}}{\text{energy lost over one cycle}} \quad (18)$$

Equation 18 can be deduced to [14]:

$$Q = \frac{f_0}{\Delta f} = \frac{\omega_0}{\Delta \omega} \quad (19)$$

Where f_0 and Δf are the resonance frequency and the full-width value of the resonance profile ($\omega_0 = 2\pi f_0$ and $\Delta \omega = 2\pi \Delta f$). The full width is measured between the points where

the amplitude of the resonance profile is at $1/\sqrt{2}$ the peak value amplitude (half-maximum values of the intensity). Therefore, Δf is also called the full width at half maximum (FWHM)[14]. For our resonator, $Q \approx 12$ was determined, from resonance curve of Fig. 3.4.

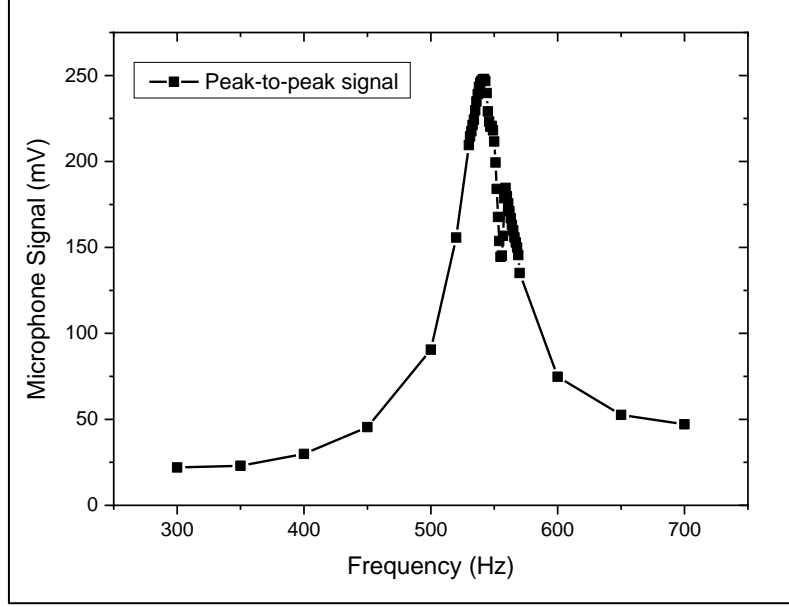


Fig. 3.4: Resonance curve of our resonator.

The resonator cavity was cut in half and a plastic holder was attached between cut edges so as to mount the microphone therein. Discontinuity of the curve at about 570 Hz is probably due to the usage of plastic holder. The standing wave patterns and resonance frequencies depend on the shape and size of the resonator. The most frequently used resonator is the cylinder, the symmetry of which coincides with that of a laser beam propagating along the cylinder axis. The acoustic resonance frequencies of a cylinder-shaped resonator with open-open ends can be obtained from Equation 20[14]:

$$f_0 = \frac{c_s}{2(L + \Delta L)} \quad (20)$$

where L is the length of the cylinder and c_s is the sound velocity. ΔL is the so-called end correction and $\Delta L \approx 0.6r$, where r is the radius of the cylinder. In our experimental setup, $L=30$ cm and $r=12$ mm, thus resulting in a resonance frequency of about 550 Hz (sound velocity is $c_s=343$ m/s in the air for 20 °C).

As a signal detector, a **MEMS-type microphone** with output sensitivity of -32 dBV (ICS-40720, InvenSense, San Jose, CA, USA) attached on the middle of the resonator cylinder cavity, collected the pressure fluctuations resulting from the PA effect. It was vital that the detector had as small dimensions as possible to be embodied in the cavity and not affect the shape of it. In order to focus the laser beam in the vicinity of the microphone, a quartz-made **focusing lens** with $f=400$ mm, was placed after the chopper.

A ***lock-in amplifier*** was necessary to achieve signal from the PA spectroscopic method. The microphone signal was introduced into a dual-phase digital lock-in amplifier (LIA-200MVD-H, Femto, Berlin, Germany) which extracted the weak signal from the background and amplified it. In general, lock-in amplifiers are used to detect and measure very small signals, all the way down to a few nanovolts. Accurate measurements may be made even when the small signal is obscured by noise sources many thousands of times larger. Lock-in amplifiers single out the component of the signal at a specific reference frequency, given by the mechanical chopper. Noise signals, at frequencies other than the reference frequency, are rejected and do not affect the measurement[21]. The integration time (time constant) of the lock-in amplifier must be considerably longer than the period of the chopper's modulation frequency to achieve maximum sensitivity for detecting weak signal[22]. The time constant of the lock-in amplifier was set to 1 s in our case to achieve longer integration times and a higher detection limit.

Nitrogen served as buffer gas so that pressure fluctuations would reach the detector. Apparently, light is able to travel through vacuum and reach the detector, as was done in TDLAS measurements, unlike sound which needs necessarily a medium so that it propagates. Hence, photoacoustic cell was loaded with nitrogen up to 1 atm total pressure. Choice of nitrogen did not come without thought as it is an inert, harmless and low-cost gas.

In PAS measurements, a certain quantity of analyzed gas was injected in the photoacoustic cell, after the latter had been evacuated from the vacuum pump. Then, nitrogen was injected to load the cell up to 1 atm total pressure. Chopped laser beam at a certain frequency interacted with the absorbing species and thus pressure fluctuations reached the microphone. Emerging signal, after having been extracted by the lock-in amplifier, was transferred to a personal computer, through an oscilloscope. An average of 8 scans was collected for every single measurement.

As well as TDLAS measurements, a linearly rising ramp was applied to the laser, so that wavelength changes with temperature, resulting in a scanning of the area of absorbance peaks. PAS measurements differed with those of TDLAS, in that no background was measured, as the photoacoustic detection is rather a direct monitor of the nonradiative relaxation channels.

3.3 Hybrid TDLAS-TDLPAS Experimental Setup and Method

The schematic of Fig. 3.5 depicts the Hybrid TDLAS-PAS experimental setup. Components have been previously presented in detail. Below, only experimental method is described. In this hybrid experimental setup, both spectroscopic techniques were employed *under same experimental conditions* for a more accurate comparison. The process started with the TDLAS measurement and acquiring of the background, which now was conducted including buffer gas inside the photoacoustic cell.

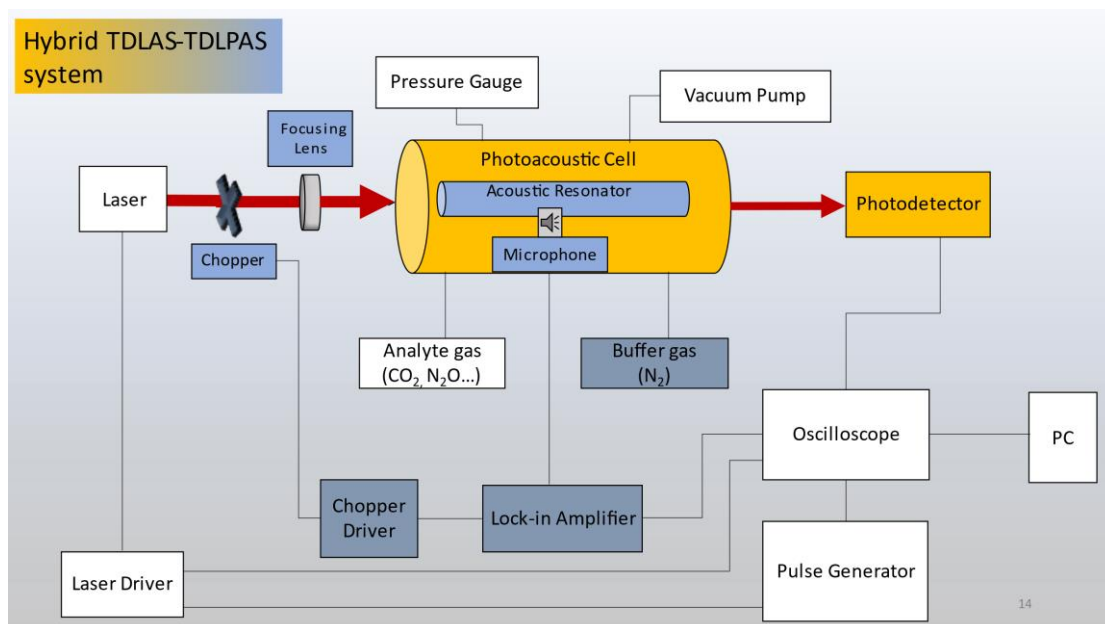


Fig. 3.5: Schematic diagram of Hybrid TDLAS-TDLPAS experimental setup

The cell was then evacuated and re-injected, firstly with the absorbing species and right afterwards with nitrogen, at a total pressure of 1 atm. Signal measurement followed and data was collected through the oscilloscope to a personal computer. During the aforementioned process, components such as chopper, lock-in amplifier and microphone remained out of use.

For the incoming PAS measurement, chopper, lock-in amplifier and microphone were activated and photodetector was deactivated, without any change in the photoacoustic cell. Data was transferred via the oscilloscope to a personal computer. An average of 8 scans was collected for every single measurement.

4. Results and Discussion

4.1. Gases under investigation

Absorbing analytes probed during the experimental processes show characteristic vibration lines in the proper laser emission wavelength. A brief assignment of these lines follows below.

- Nitrous oxide (N-N-O) has three fundamental infrared active absorption bands: $\nu_1 = 1285 \text{ cm}^{-1} \sim 7.8 \text{ }\mu\text{m}$ (N-O stretching), $\nu_2 = 589 \text{ cm}^{-1} \sim 17 \text{ }\mu\text{m}$ (N-N-O bending) and $\nu_3 = 2224 \text{ cm}^{-1} \sim 4.5 \text{ }\mu\text{m}$ (N-N stretching). The gas has overtones of the fundamental absorption bands and ro-vibrational transitions in the near-infrared region (1-2 μm). In our case, a multi-line band of 2nd overtone of ν_3 fundamental vibration ($3\nu_3$) was investigated[23], [24].
- Ammonia has four fundamental infrared active absorption bands, two of which are degenerate: $\nu_1 = 3223 \text{ cm}^{-1} \sim 2.96 \text{ }\mu\text{m}$ (N-H symmetric stretching), $\nu_2 = 1060 \text{ cm}^{-1} \sim 9.43 \text{ }\mu\text{m}$ (N-H symmetric bending), $\nu_3 = 3378 \text{ cm}^{-1} \sim 3.01 \text{ }\mu\text{m}$ (N-H asymmetric stretching) and $\nu_4 = 1646 \text{ cm}^{-1} \sim 2.96 \text{ }\mu\text{m}$ (N-H asymmetric bending). Degeneracy occurs when two bending modes, orthogonal to each other, vibrate with the same energy. Besides the fundamental stretching and bending modes that appear in the IR spectrum, other transitions can also appear such as *combination bands* (two or more fundamental modes added together). The multitude of lines examined is a result of coincidence of several overtone and combination bands at 1.52 μm , including $\nu_1 + \nu_3$ and $2\nu_3$ bands[25], [26].
- For acetylene we have seven normal modes of vibration. Two of these modes are doubly degenerate, hence giving five distinct fundamental frequencies. Acetylene has two fundamental infrared active absorption bands: ν_3 at $3294.8 \text{ cm}^{-1} \sim 3.03 \text{ }\mu\text{m}$ (asymmetric C-H stretching) and ν_5 at $730.3 \text{ cm}^{-1} \sim 13.7 \text{ }\mu\text{m}$ (symmetric H-C-C-H bending). The remaining $\nu_1 = 3372.8 \text{ cm}^{-1} \sim 2.96 \text{ }\mu\text{m}$ (symmetric C-H stretching), $\nu_2 = 1974.3 \text{ cm}^{-1} \sim 5.06 \text{ }\mu\text{m}$ (symmetric C-C stretching) and $\nu_4 = 612.9 \text{ cm}^{-1} \sim 16.33 \text{ }\mu\text{m}$ (asymmetric H-C-C-H bending) vibration modes are IR inactive (Raman active). In this experiment, the combination band of the two stretching (asymmetric and symmetric) $\nu_1 + \nu_3$ modes at $6500\text{-}6600 \text{ cm}^{-1}$ was investigated[27]–[29].
- Carbon dioxide exhibits four normal modes of vibration, with one being doubly degenerate. It has two fundamental infrared active absorption bands: ν_2 at $667 \text{ cm}^{-1} \sim 14.99 \mu\text{m}$ (O-C-O bending) and ν_3 at $2349 \text{ cm}^{-1} \sim 4.25 \mu\text{m}$ (asymmetric C-O stretching). The remaining $\nu_1 = 1333 \text{ cm}^{-1} \sim 7.50 \mu\text{m}$ (symmetric C-O stretching) vibration mode is IR inactive (Raman active). The multitude of lines examined is a result of $3\nu_1 + \nu_3$ combination bands at 1.57 μm [30], [31].

- Methane shows nine vibrational modes, where two of them are triply degenerate and one is doubly degenerate. Thus, four distinct fundamental frequencies occur: $\nu_1=2917\text{ cm}^{-1}\sim 3.42\mu\text{m}$ (symmetric C-H stretching), $\nu_2=1534\text{ cm}^{-1}\sim 6.51\mu\text{m}$ (C-H bending /" twisting"), $\nu_3=3019\text{ cm}^{-1}\sim 3.31\mu\text{m}$ (asymmetric C-H stretching) and $\nu_4=1306\text{ cm}^{-1}\sim 7.65\mu\text{m}$ (C-H bending /" scissoring"). In our investigation, a single line deriving from the 1st overtone of ν_3 fundamental frequency ($2\nu_3$) was examined[32]–[35].

Multitude of lines in spectra of the analyzed gases is attributed to the *fine structure* of vibrational spectrum. In such a narrow spectral scanning range of lasers employed, what we observe are *ro-vibrational* transitions. That is, transitions involving changes in both vibrational and rotational states. Changes in rotational energy levels are typically much smaller than changes in vibrational energy levels. Both the ground and excited vibrational states contain sequences of quantized rotational levels. The spectra are often resolved into *lines* due to transitions from one rotational level in the ground vibrational state to one rotational level in the vibrationally excited band (Fig. 4.1). The lines corresponding to a given vibrational transition form a *band*.

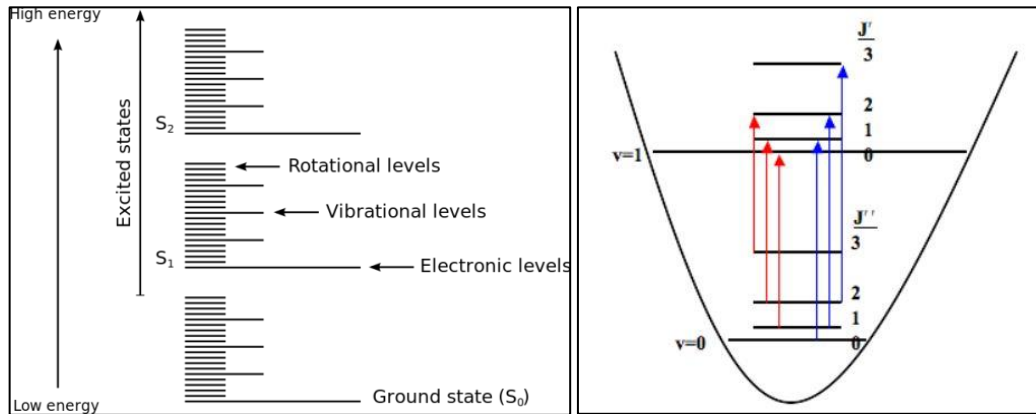


Fig. 4.1: (left) Ground and excited states of rotational, vibrational and electronic levels of a gas molecule (adapted from [36]) (right) Rotational transitions of the molecule between the ground and first excited vibrational states (J'' and J' refer to rotational levels of ground and first excited vibration states)(adapted from [37])

4.2 TDLAS Results

❖ Methane (CH_4)

A laser emitting at 1653.7 nm (6047 cm^{-1}) with a scanning range of about 8 cm^{-1} ($6043\text{--}6051\text{ cm}^{-1}$) was employed for CH_4 measurements. Ramp duration was set at 19 seconds for optimum recording time and laser diode current was set at a stable value of 110 mA.

Figure 4.2.1 depicts the temperature ramp, initial light intensity (baseline) and transmitted light intensity (signal) for CH₄ measurements.

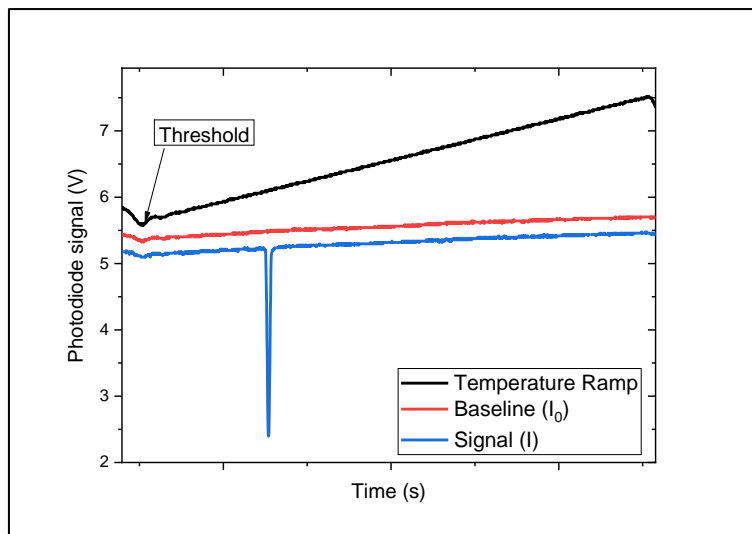


Fig. 4.2.1: Temperature ramp, Initial light intensity (baseline) and Transmitted light intensity (signal) for CH₄

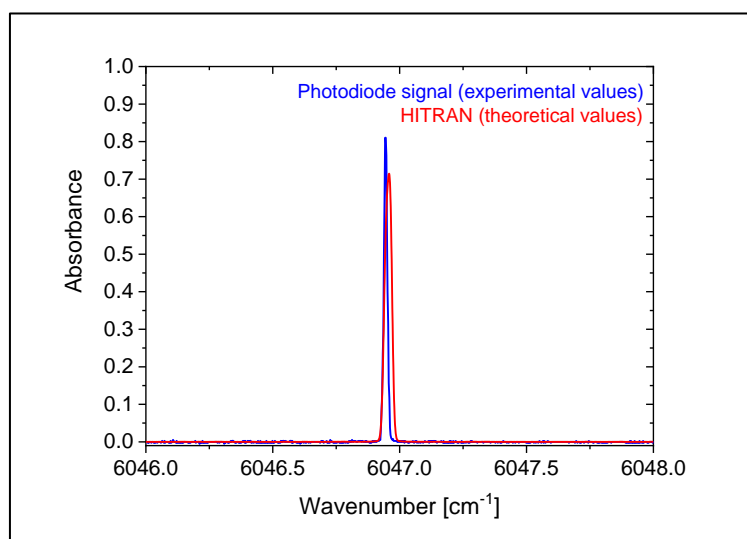


Fig. 4.2.2: Normalized [0,1] Experimental and Theoretical (HITRAN) CH₄ absorbance spectra

After the acquisition of baseline and signal, absorbance, $\alpha = \ln(I_0/I)$, was calculated for all 6 different certain-pressure quantities injected one at a time in the gas cell (10, 8, 6, 4, 2, 1 mbar). A calibration of wavenumbers on x-axis was performed using the HITRAN spectra database for this as well as all acquired spectra following. For methane, in the spectral range provided by the laser, a single peak at 6046.94 cm⁻¹ was acquired (Fig. 4.2.2).

❖ ii) Carbon Dioxide (CO_2)

For CO_2 measurements, a laser emitting at 1572 nm (6361 cm^{-1}) with a scanning range of about 8 cm^{-1} ($6363\text{-}6371 \text{ cm}^{-1}$) was used. Ramp duration was set at 19 seconds and laser diode current was set at a stable value of 100 mA. Figure 4.2.3 depicts the temperature ramp, initial light intensity (baseline) and transmitted light intensity (signal) for CO_2 measurements. Absorbance was calculated for CO_2 at pressures of: 60, 50, 25, 20, 15 and 10 mbar. CO_2 has a multi-line band, consisting of 6 main peaks in the spectral range covered by the laser (Fig 4.2.4).

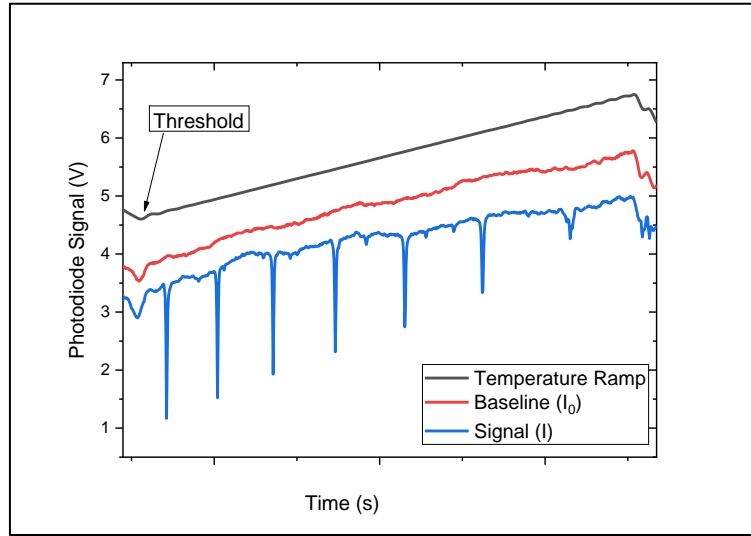


Fig. 4.2.3: Temperature ramp, Initial light intensity (baseline) and Transmitted light intensity (signal) for CO_2

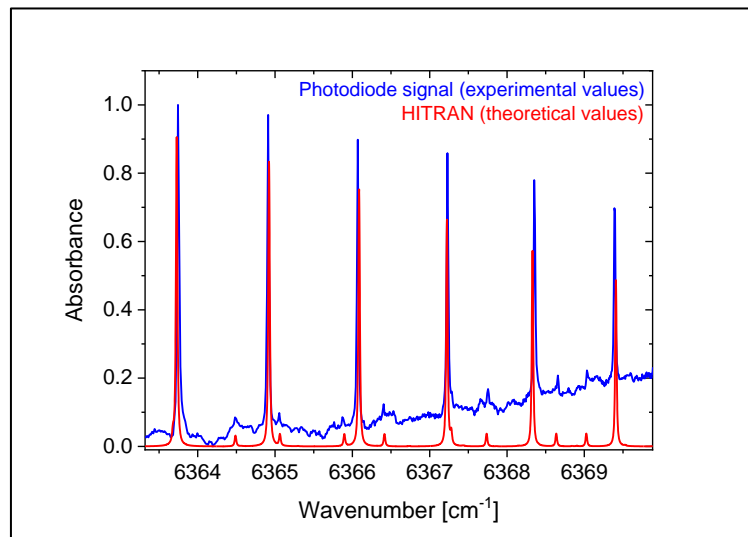


Fig. 4.2.4: Normalized [0,1] Experimental and Theoretical (HITRAN) CO_2 absorbance spectra

❖ iii) Acetylene (C_2H_2)

Acetylene was measured with a laser emitting at 1521 nm (6574 cm^{-1}) with a scanning range of about 8 cm^{-1} ($6567\text{--}6575\text{ cm}^{-1}$). Ramp duration was set at 19 seconds and laser diode current was set at a stable value of 100 mA. Figure 4.2.5 depicts the temperature ramp, initial light intensity (baseline) and transmitted light intensity (signal) for C_2H_2 measurements. Absorbance was calculated for C_2H_2 at pressures of: 1.5, 1, 0.7, 0.5, 0.3, 0.2, 0.08, 0.06 mbar. C_2H_2 has a multi-line band, consisting of 4 main peaks in the spectral range covered by the laser (Fig. 4.2.6).

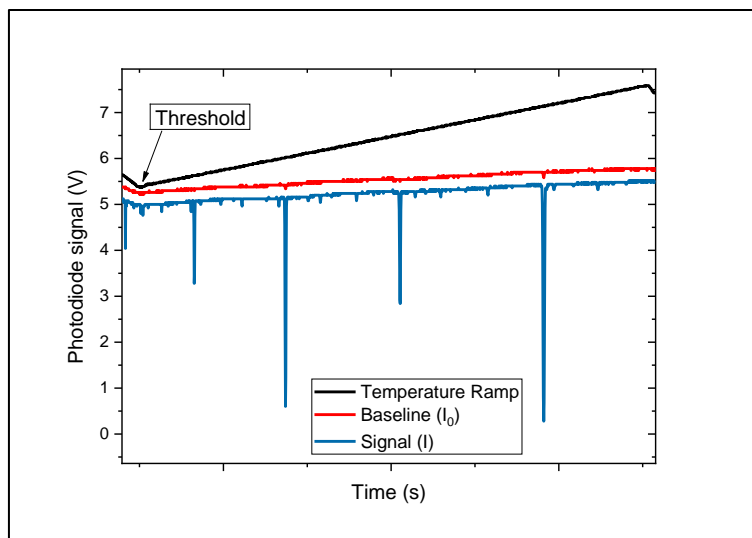


Fig. 4.2.5: Temperature ramp, Initial light intensity (baseline) and Transmitted light intensity (signal) for C_2H_2

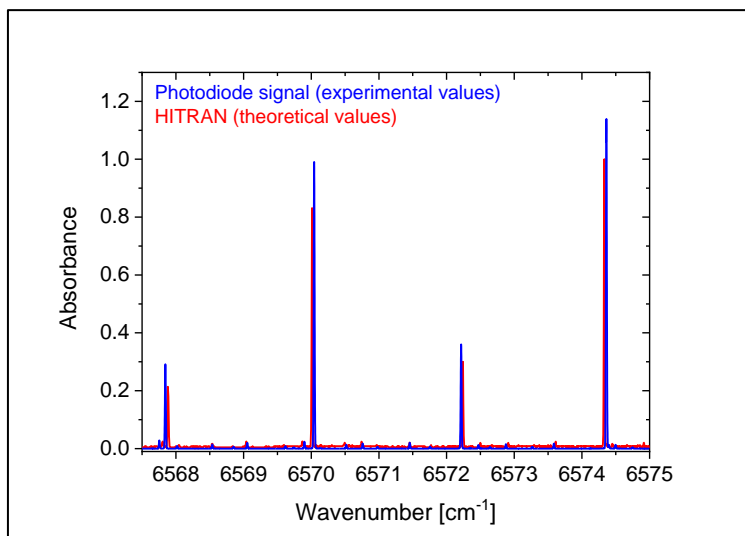


Fig. 4.2.6: Experimental and Theoretical (HITRAN) C_2H_2 absorbance spectra

❖ iv) Nitrous Oxide (N_2O)

Nitrous oxide was measured with same laser as acetylene, emitting at 1521 nm (6574 cm^{-1}) with a scanning range of about 8 cm^{-1} ($6567\text{--}6575\text{ cm}^{-1}$). Ramp duration was set at 19 seconds and laser diode current was set at a stable value of 100 mA. Figure 4.2.7 depicts the temperature ramp, initial light intensity (baseline) and transmitted light intensity (signal) for N_2O measurements. Absorbance was calculated for N_2O at pressures of: 74, 73, 47, 17, 8.6 mbar. N_2O has a multi-line band, consisting of 9 main peaks in the spectral range covered by the laser (Fig. 4.2.8).

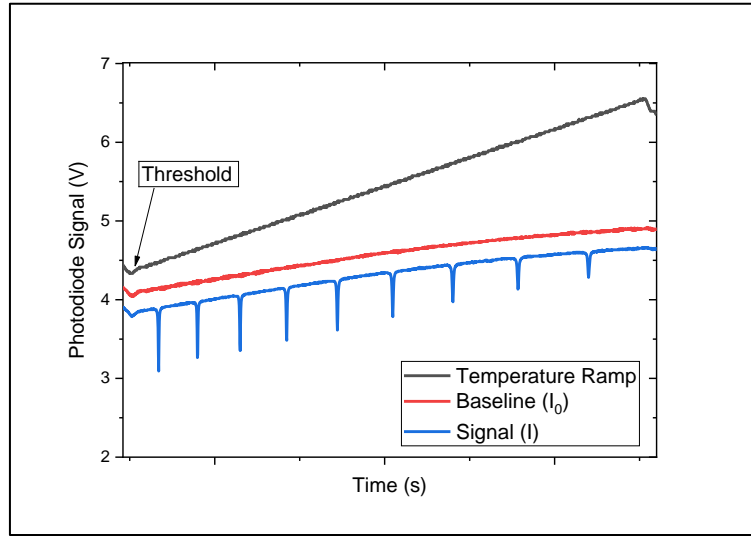


Fig. 4.2.7: Temperature ramp, Initial light intensity (baseline) and Transmitted light intensity (signal) for N_2O

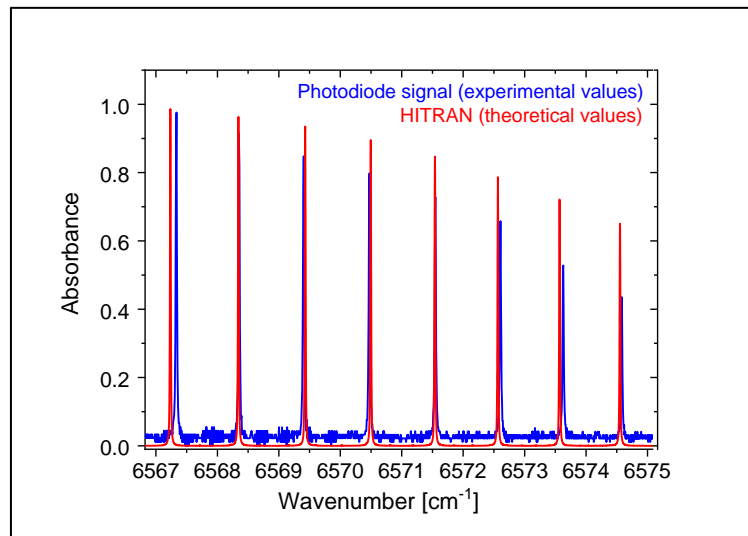


Fig. 4.2.8: Normalized [0,1] Experimental and Theoretical (HITRAN) N_2O absorbance spectra

❖ ν) Ammonia (NH_3)

Ammonia was the 3rd gas measured with the laser emitting at 1521 nm (6574 cm^{-1}) with a scanning range of about 8 cm^{-1} ($6567\text{-}6575 \text{ cm}^{-1}$). Ramp duration was set at 19 seconds and laser diode current was set at a stable value of 100 mA. Figure 4.2.9 depicts the temperature ramp, initial light intensity (baseline) and transmitted light intensity (signal) for NH_3 measurements. Absorbance was calculated for NH_3 at pressures of: 5, 4, 3, 2, 1 mbar. NH_3 has a multi-line band, consisting of 2 main peaks in the spectral range covered by the laser (Fig. 4.2.10).

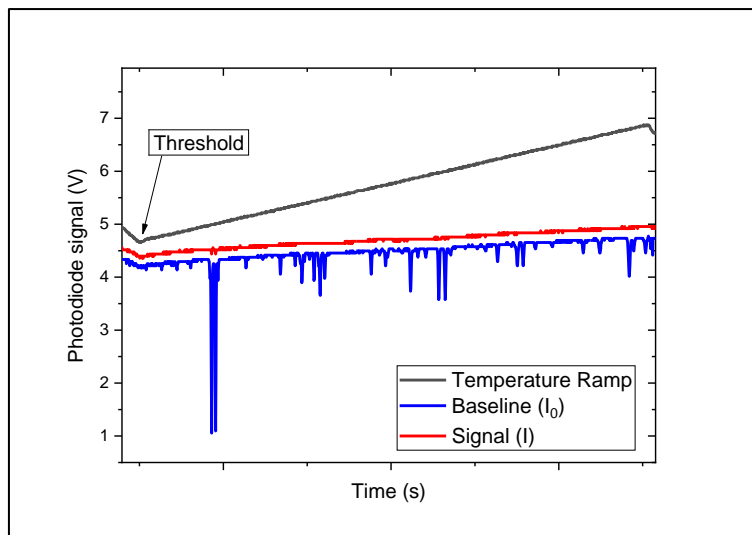


Fig. 4.2.9: Temperature ramp, Initial light intensity (baseline) and Transmitted light intensity (signal) for NH_3

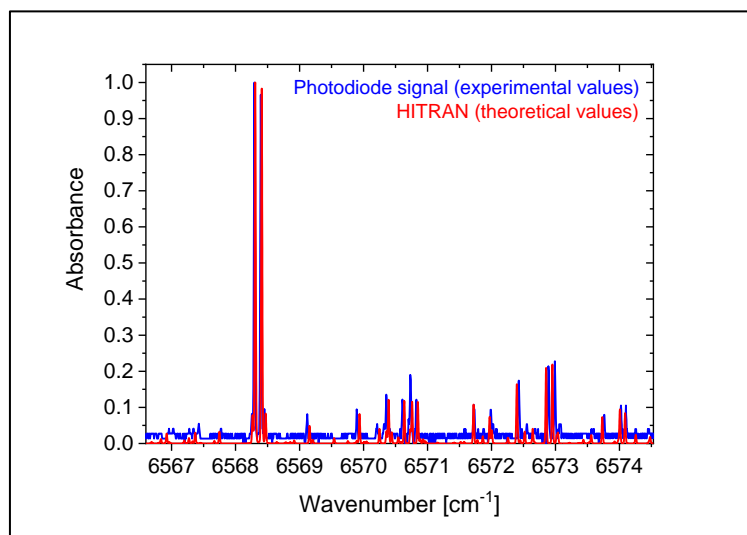


Fig. 4.2.10: Normalized [0,1] Experimental and Theoretical (HITRAN) NH_3 absorbance spectra

4.3 TDLPAS Results

❖ Carbon Dioxide (CO_2)

For CO_2 measurements, the same laser as TDLAS, emitting at 1572 nm (6361 cm^{-1}) was used. Scanning range though was different than TDLAS measurements as a different laser diode current was applied. A stable value of 300 mA led to the shift of scanning range to $6358\text{-}6365 \text{ cm}^{-1}$. Ramp duration was set at 49 seconds for optimum recording time. CO_2 photoacoustic signal was measured at pressures of: 100, 88, 79, 69, 59, 50, 42, 30, 21, 15 mbar. CO_2 has a multi-line band, consisting of 5 main peaks in the spectral range covered by the laser in the scanning range (Fig 4.3.1).

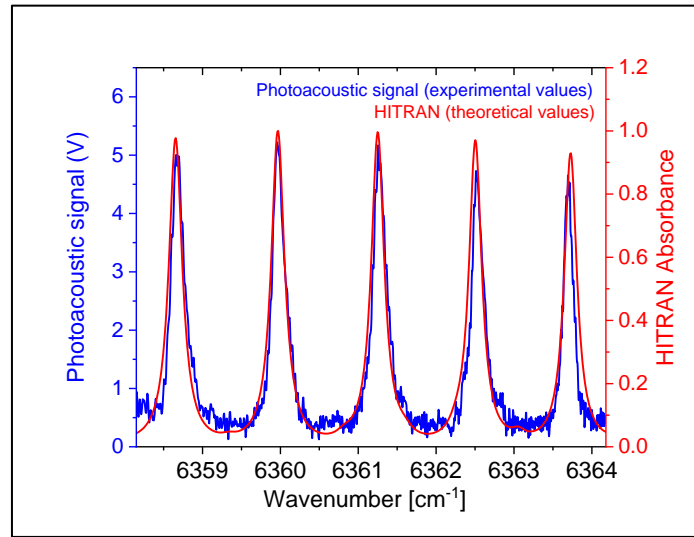


Fig. 4.3.1: Experimental (Photodiode signal) and Theoretical (HITRAN) CO_2 absorbance spectra

❖ ii) Acetylene (C_2H_2)

Acetylene was measured with a laser emitting at 1520 nm (6578 cm^{-1}), different than the one acquiring TDLAS spectra, with a scanning range of about 9 cm^{-1} ($6571\text{-}6580 \text{ cm}^{-1}$). Ramp duration was set at 49 seconds and laser diode current was set at a stable value of 100 mA. C_2H_2 photoacoustic signal was measured at pressures of: 33, 21, 11, 5, 1 mbar. C_2H_2 has a multi-line band, consisting of 4 main peaks in the laser spectral range (Fig 4.3.2).

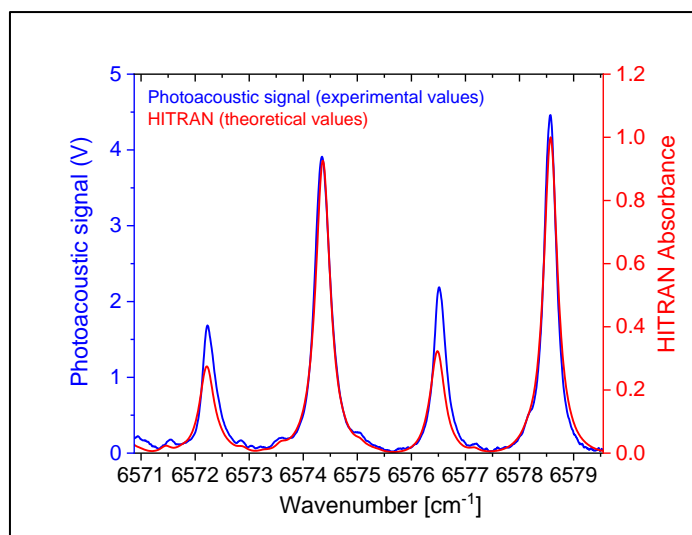


Fig. 4.3.2: Experimental (Photodiode signal) and Theoretical (HITRAN) C_2H_2 absorbance spectra

❖ iii) Nitrous Oxide (N_2O)

Nitrous oxide was measured with same laser as acetylene, emitting at 1520 nm (6578 cm^{-1}) with a scanning range of about 9 cm^{-1} ($6571\text{--}6580\text{ cm}^{-1}$). Ramp duration was set at 49 seconds and laser diode current was set at a stable value of 100 mA. N_2O photoacoustic signal was measured at pressures of: 800, 400, 200, 100 mbar. N_2O has a multi-line band, consisting of 8 main peaks in the laser spectral range (Fig 4.3.3).

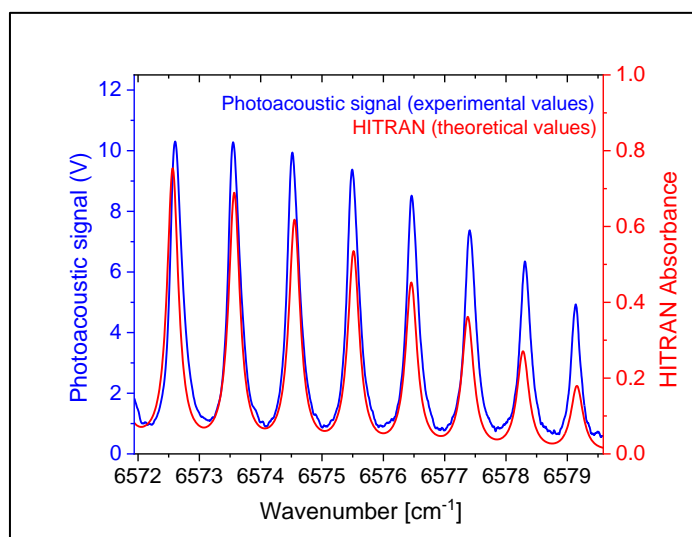


Fig. 4.3.3: Experimental (Photodiode signal) and Theoretical (HITRAN) N_2O absorbance spectra

❖ iv) Ammonia (NH_3)

Ammonia was the 3rd gas measured with the laser emitting at 1520 nm (6578 cm^{-1}) with a scanning range of about 9 cm^{-1} ($6571\text{-}6580 \text{ cm}^{-1}$). Ramp duration was set at 49 seconds and laser diode current was set at a stable value of 100 mA. NH_3 photoacoustic signal was measured at pressures of: 90, 40, 31, 20, 13, 7 mbar. NH_3 has a multi-line band in the laser spectral range consisting of several peaks, with the one at 6579 cm^{-1} being the dominant (Fig 4.3.4).

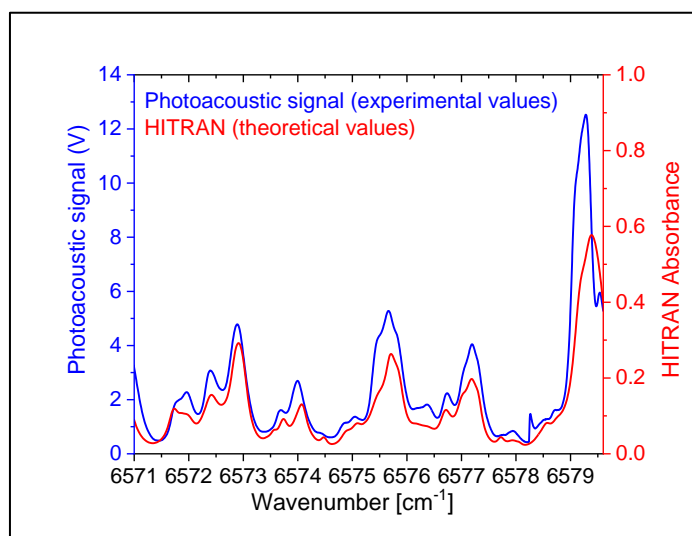


Fig. 4.3.4: Experimental (Photodiode signal) and Theoretical (HITRAN) NH_3 absorbance spectra

4.4 Hybrid TDLAS-TDLPAS Results

Ammonia was the only gas measured with the laser emitting at 1520 nm (6578 cm^{-1}), with a scanning range of about 9 cm^{-1} ($6571\text{-}6580 \text{ cm}^{-1}$), in the hybrid system. Ramp duration was set at 49 seconds and laser diode current was set at a stable value of 100 mA. NH_3 signals for both techniques were measured at pressures of: 51, 43, 33, 21, 10 and 5.2 mbar. (Fig 4.4.1).

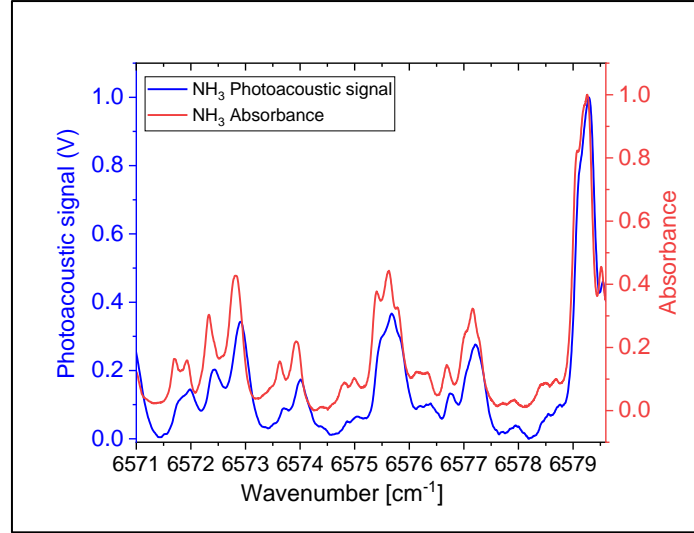


Fig. 4.4.1: Experimental photoacoustic signal and photodiode (absorbance) signal spectra of NH_3 from hybrid system

4.5 Data Processing

In all data acquired, a baseline correction and a Voigt fit function was applied via the use of Origin 2018 to certain selected peaks of spectra, in order to extract a *peak height value*, corresponding to measured absorbance. As far as the Voigt function of spectral line shape is concerned, the profile of a spectral line broadened both by *thermal motion* of the atoms of the light source and by *collisions* that interrupt the radiation (the so-called broadening effects) is given, on the assumption that those two processes are independent, by the convolution of Gaussian and Lorentzian functions known as a Voigt function[38]. Selected peaks in multi-line bands were those with maximum absorbance, compared to the rest of spectrum. Moreover, a least-squares regression (linear fit) was applied for “measured pressure” (x-axis) and “experimental peak height” (y axis). The aim of this processing was to obtain the LLD (lower limit of detection) for the two spectroscopic techniques used for probing of analytes. LLD was determined through the *calibration method*[39]. In this method the standard error of the y-estimate for the least-squares regression line, $S_{y/x}$ is used. $S_{y/x}$ is a measure of the average deviation of the experimental values from the regression line, as given by Equation 21[39]:

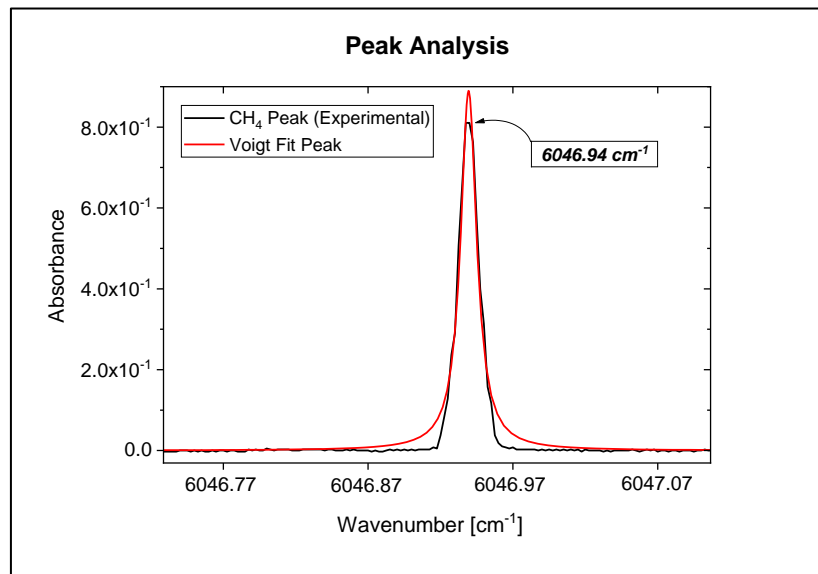
$$S_{y/x} = \sqrt{\frac{\sum(Y_i - Y_{r,i})^2}{n - 2}} \quad (21)$$

Equation 20 defines $S_{y/x}$ for a regression line fitted through the experimental points (X_i , Y_i), where X , is the concentration of analyte (pressure in our case) and Y , is the analytical signal measured by the technique. The parameters $Y_{r,i}$, and n are the analytical signal predicted by the regression line and the number of data points, respectively. The calibration plot method is able to use data over a range of concentrations, by measuring the deviation for different concentrations from a common point of reference (the regression line). The determination of the LLD by the calibration plot method is calculated from the least-squares regression parameters as shown in Equation 22[39].

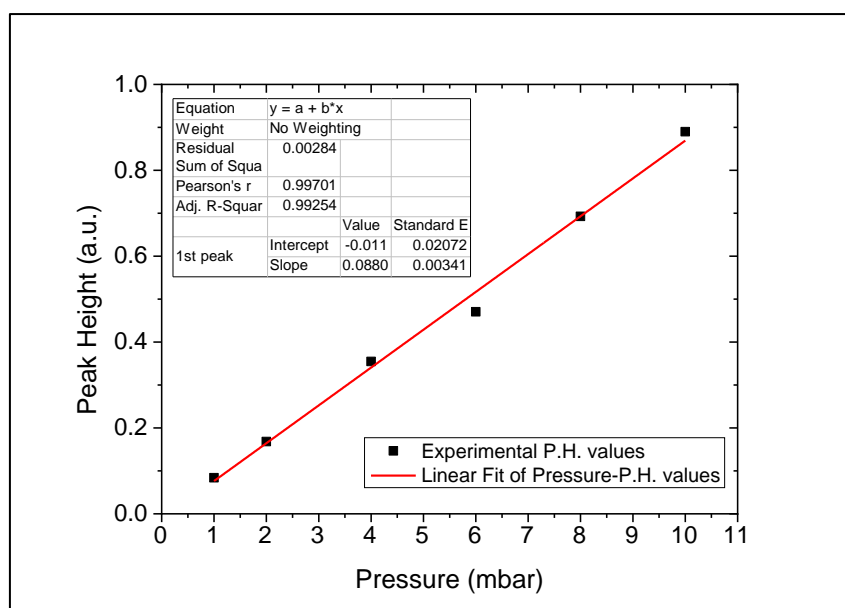
$$3S_{y/x}/\text{slope} = LLD \quad (22)$$

❖ Methane (CH_4)-TDLAS

For TDLAS measurements of methane, the single peak present in the absorption spectrum at 6046.94 cm^{-1} was used for the Voigt fit and the extraction of peak height values (Fig 4.4.1). The least-squares regression line for all measured values of pressure is shown in Fig 4.4.2.



4.5.1 Voigt fit of CH_4 peak (TDLAS)

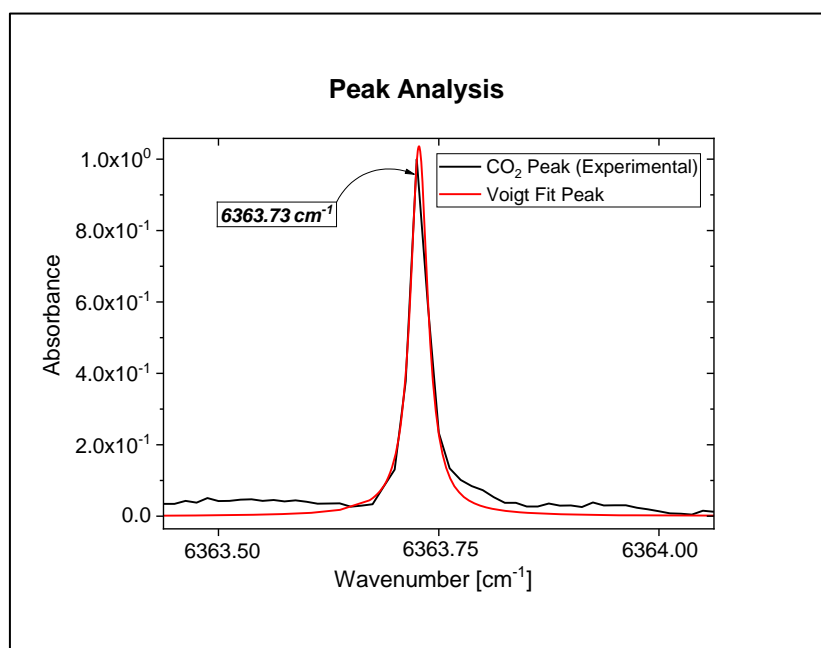


4.5.2 Least-squares regression line for CH_4 (TDLAS)

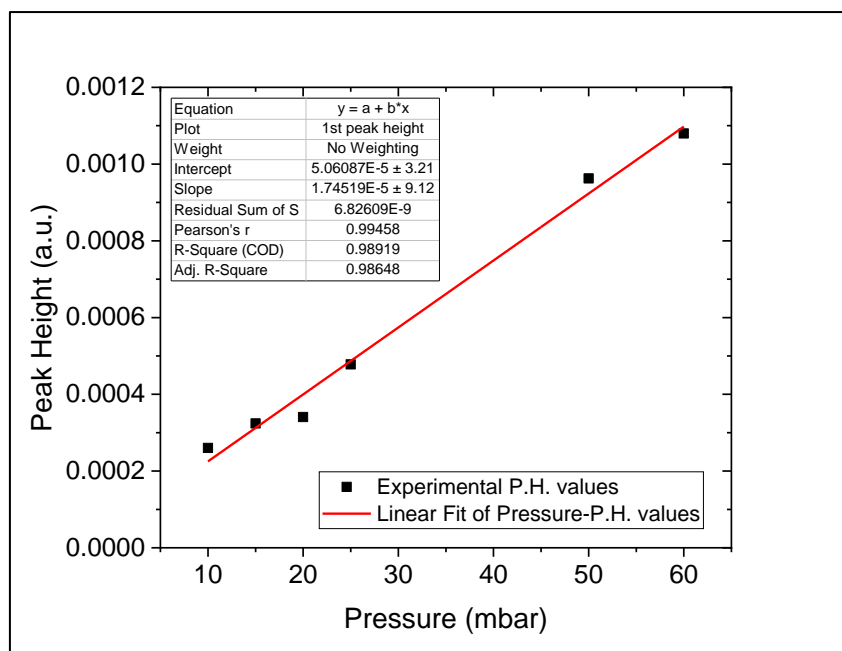
❖ ii) Carbon Dioxide (CO_2)-TDLAS & TDLPAS

CO_2 TDLAS

For carbon dioxide TDLAS measurements, the peak present at 6363.73 cm^{-1} in the absorption spectrum was used for the Voigt fit and the extraction of peak height values (Fig 4.4.3). The least-squares regression line for all measured values of pressure is shown in Fig 4.4.4.



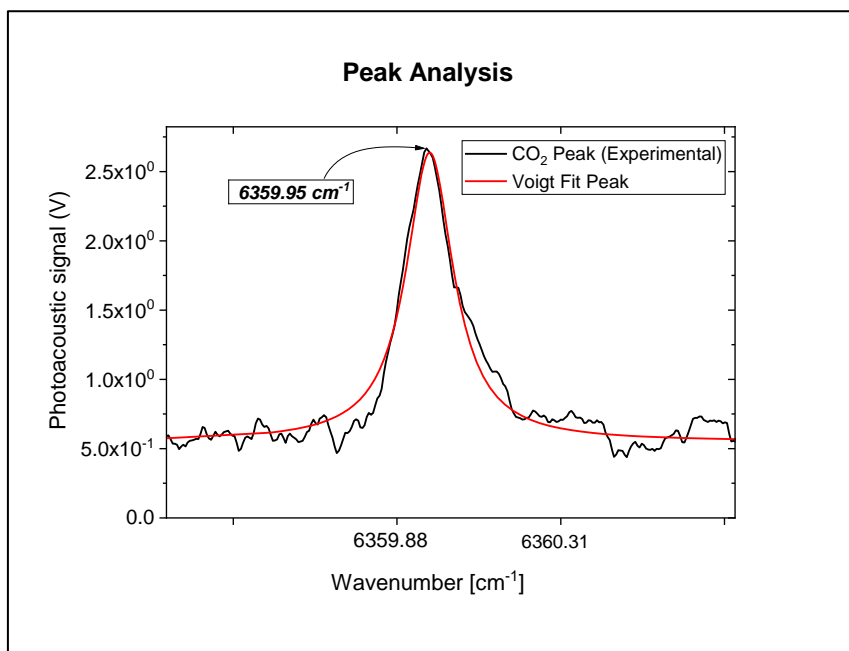
4.5.3 Voigt fit of CO_2 selected peak for TDLAS



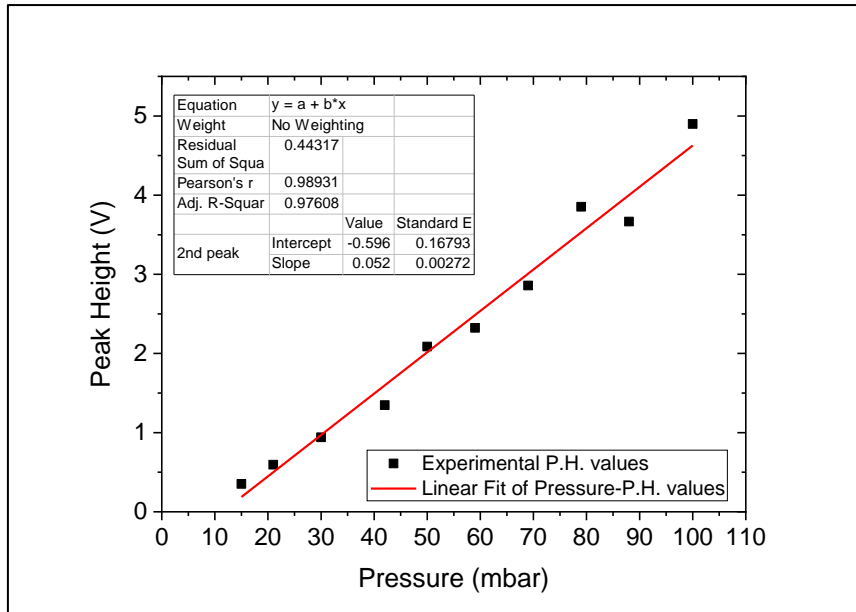
4.5.2 Least-squares regression line for CO_2 (TDLAS)

CO_2 TDLPAS

For carbon dioxide TDLPAS measurements, the peak present at 6359.95 cm^{-1} in the photoacoustic spectrum was used for the Voigt fit and the extraction of peak height values (Fig 4.4.5). The least-squares regression line for all measured values of pressure is shown in Fig 4.4.6.



4.5.5 Voigt fit of CO_2 selected peak (TDLPAS)

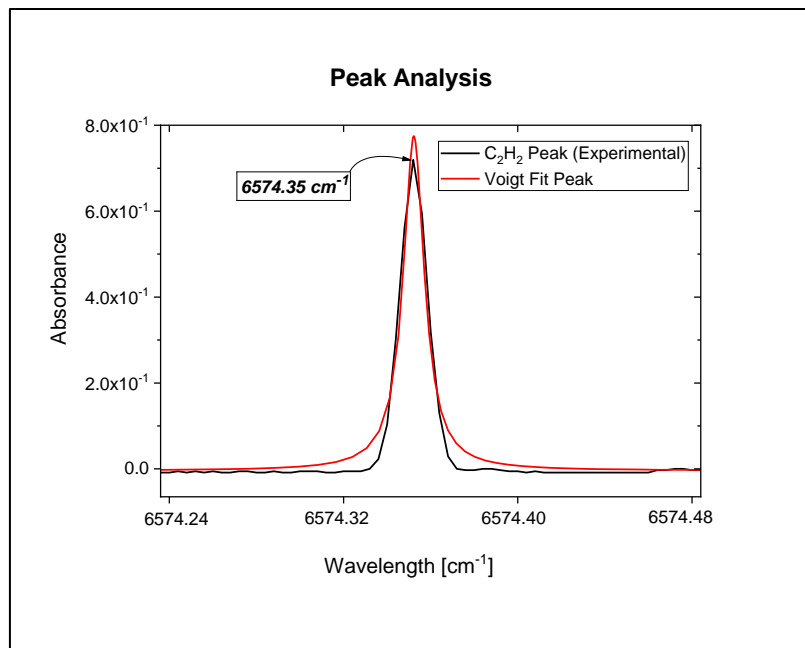


4.5.6 Least-squares regression line for CO_2 (TDLPAS)

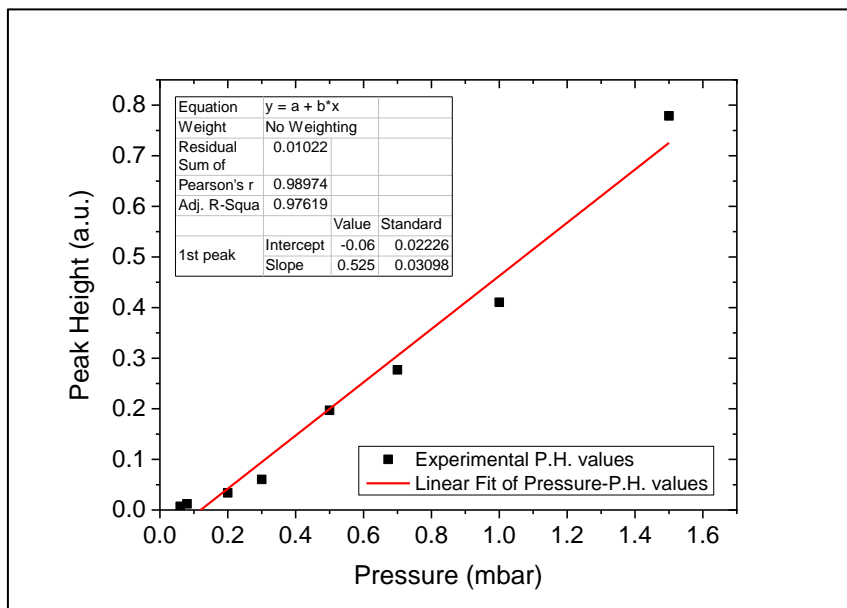
❖ iii) Acetylene (C_2H_2)- TDLAS & TDLPAS

C_2H_2 TDLAS

The peak present at 6574.35 cm^{-1} in the absorption spectrum was used for the Voigt fit and the extraction of peak height values (Fig 4.4.7), for acetylene TDLAS measurements. The least-squares regression line for all measured values of pressure is shown in Fig 4.4.8.



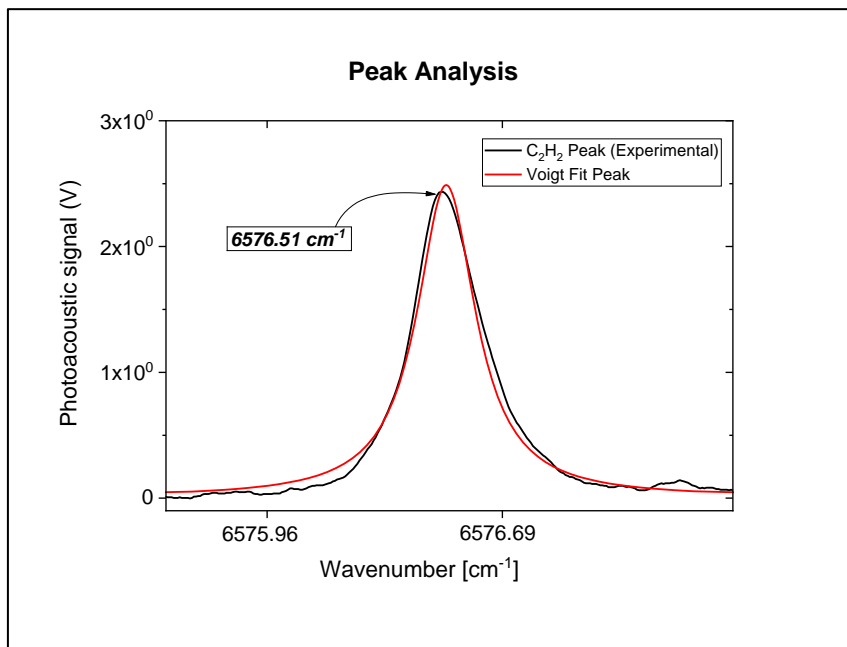
4.5.7 Voigt fit of C_2H_2 selected peak (TDLAS)



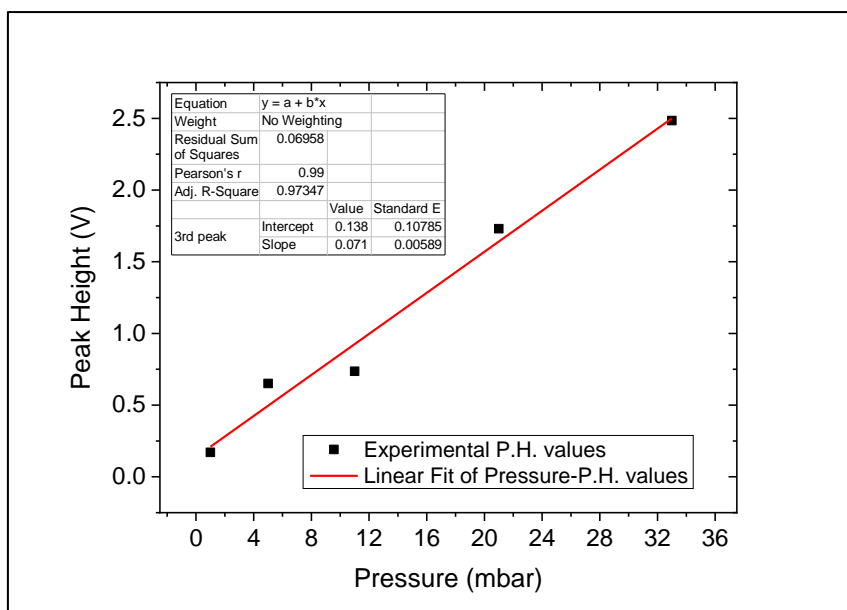
4.5.8 Least-squares regression line for C_2H_2 (TDLAS)

C_2H_2 TDLPAS

The peak present at 6576.51 cm^{-1} in the photoacoustic spectrum was used for the Voigt fit and the extraction of peak height values (Fig 4.4.9), for acetylene TDLPAS measurements. The least-squares regression line for all measured values of pressure is shown in Fig 4.4.10.



4.5.9 Voigt fit of C_2H_2 selected peak (TDLPAS)

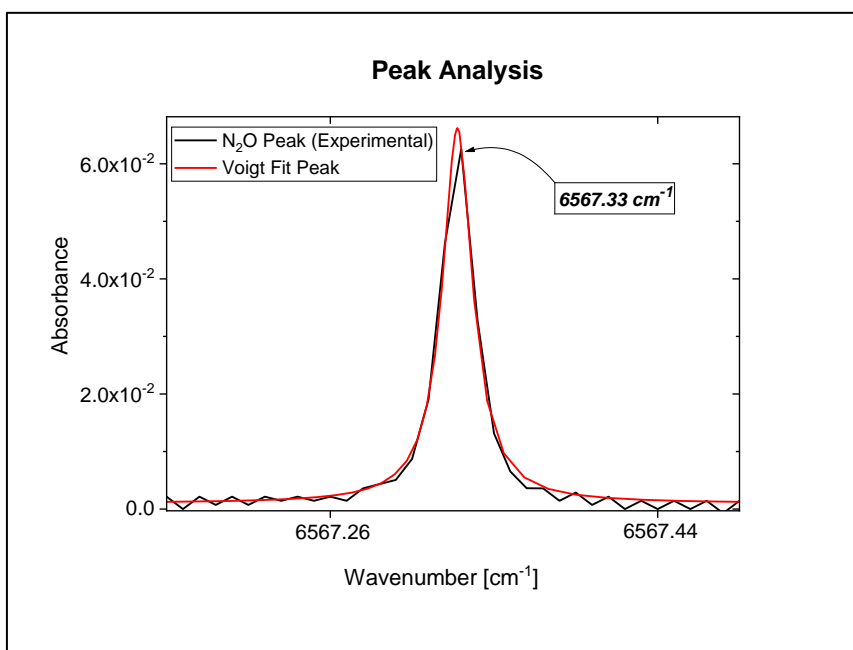


4.5.10 Least-squares regression line for C_2H_2 (TDLPAS)

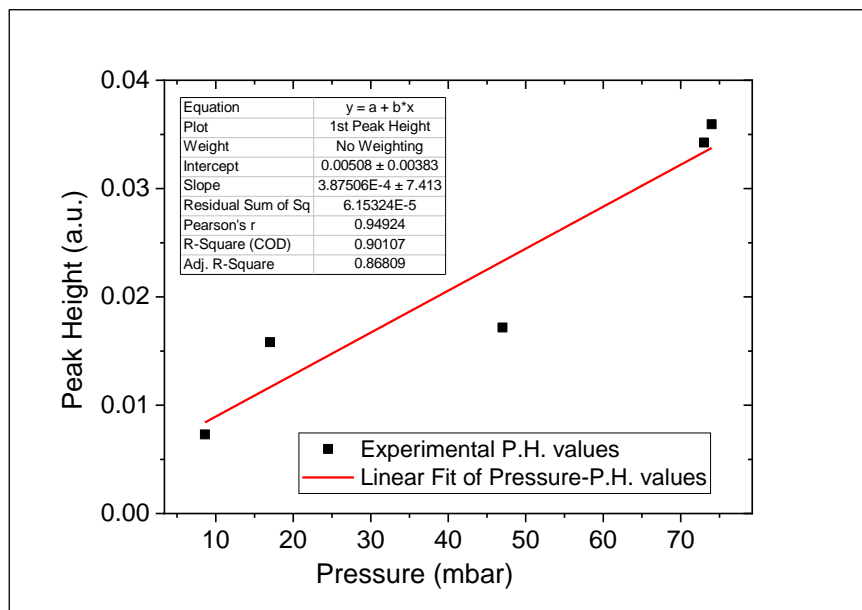
❖ Nitrous Oxide (N_2O) - TDLAS & TDLPAS

N_2O TDLAS

For TDLAS measurements of nitrous oxide, the peak present at 6567.33 cm^{-1} in the absorption spectrum was used for the Voigt fit and the extraction of peak height values (Fig 4.4.11). The least-squares regression line for all measured values of pressure is shown in Fig 4.4.12.



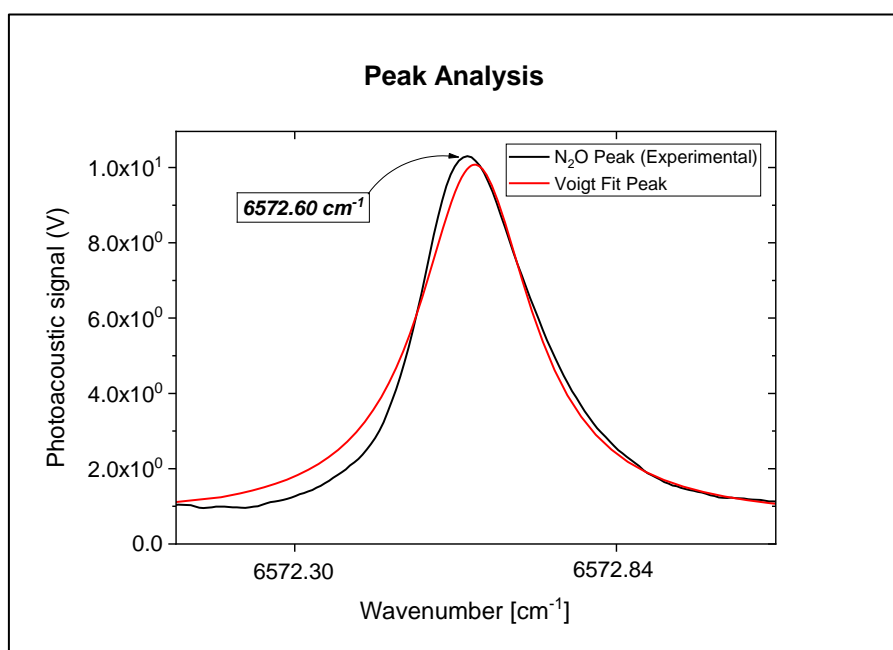
4.5.11 Voigt fit of N_2O selected peak (TDLAS)



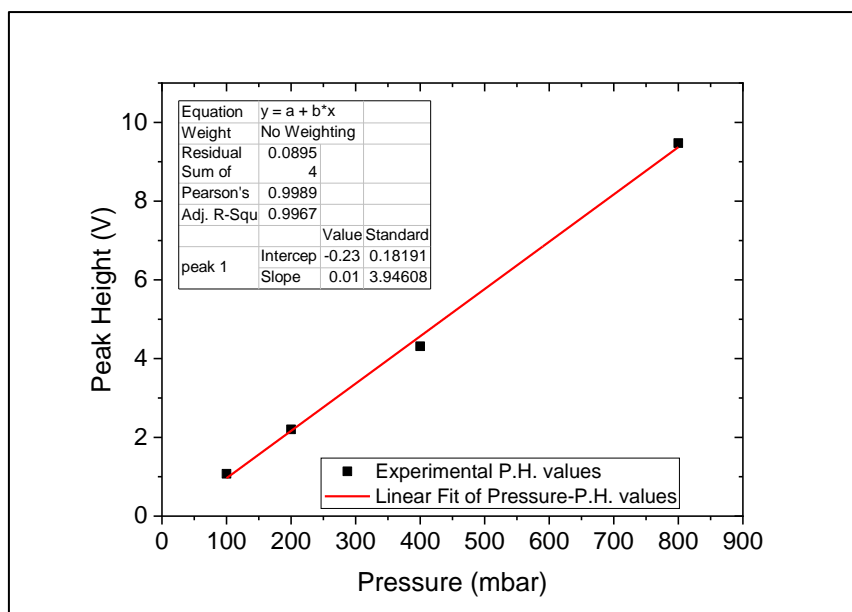
4.5.12 Least-squares regression line for N_2O (TDLAS)

N_2O TDLPAS

For TDLPAS measurements of nitrous oxide, the peak present at 6572.60 cm^{-1} in the photoacoustic spectrum was used for the Voigt fit and the extraction of peak height values (Fig 4.4.13). The least-squares regression line for all measured values of pressure is shown in Fig 4.4.14.



4.5.13 Voigt fit of N_2O selected peak (TDLPAS)

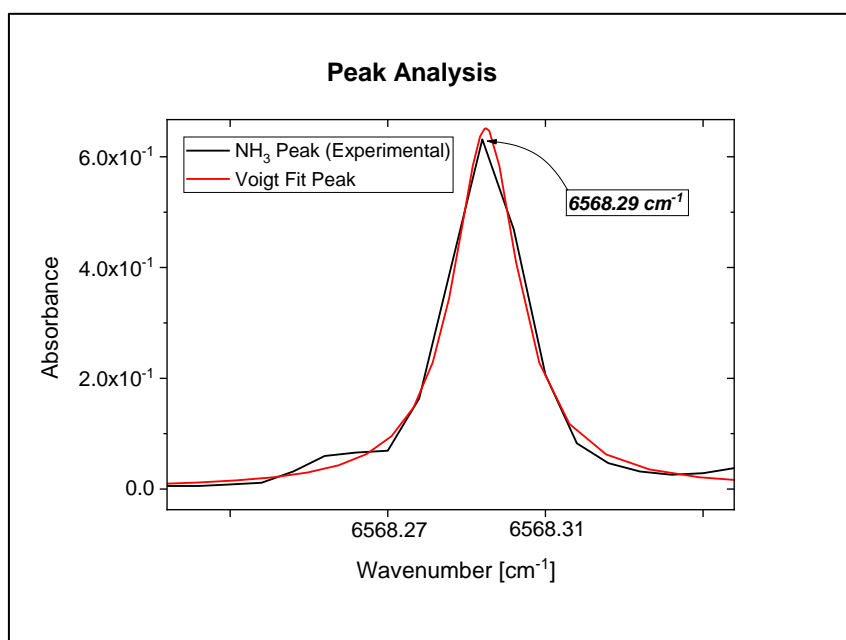


4.5.14 Least-squares regression line for N_2O (TDLPAS)

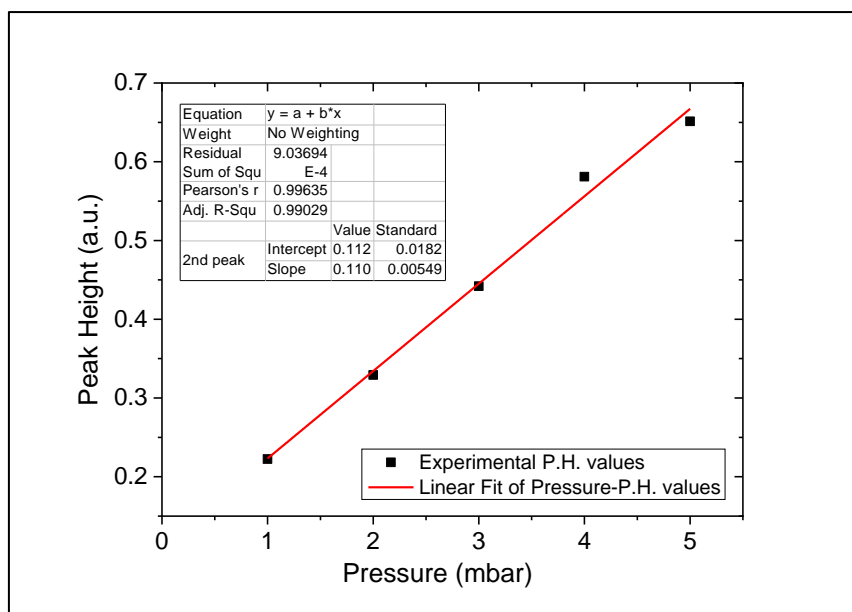
❖ Ammonia (NH_3) - TDLAS & TDLPAS

NH_3 TDLAS

The peak present at 6568.29 cm^{-1} in the absorption spectrum was used for the Voigt fit and the extraction of peak height values (Fig 4.4.15), for ammonia TDLAS measurements. The least-squares regression line for all measured values of pressure is shown in Fig 4.4.16.



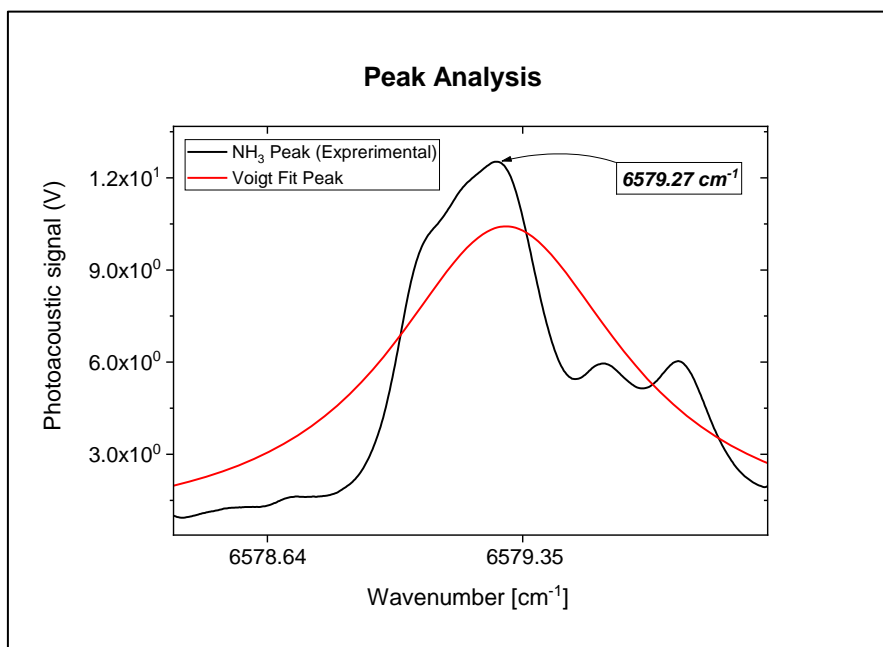
4.5.15 Voigt fit of NH_3 selected peak (TDLAS)



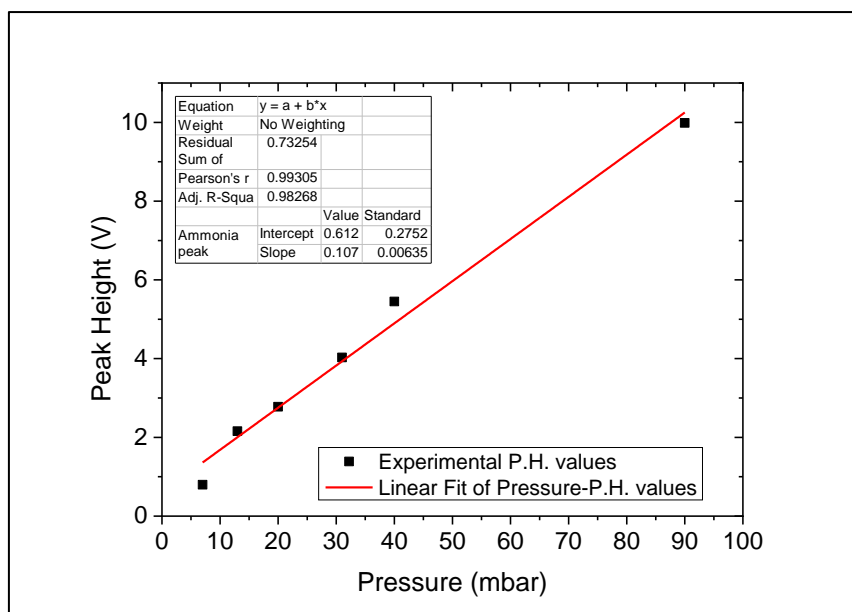
4.5.16 Least-squares regression line for NH_3 (TDLAS)

NH_3 TDLPAS

The peak present at 6579.27 cm^{-1} in the photoacoustic spectrum was used for the Voigt fit and the extraction of peak height values (Fig 4.4.17), for ammonia TDLPAS measurements. The least-squares regression line for all measured values of pressure is shown in Fig 4.4.18.



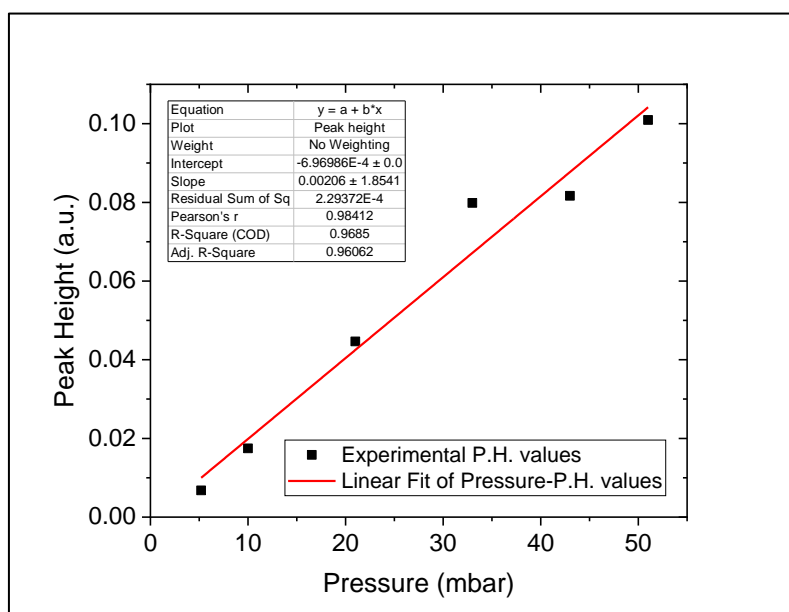
4.5.17 Voigt fit of NH_3 selected peak (TDLPAS)



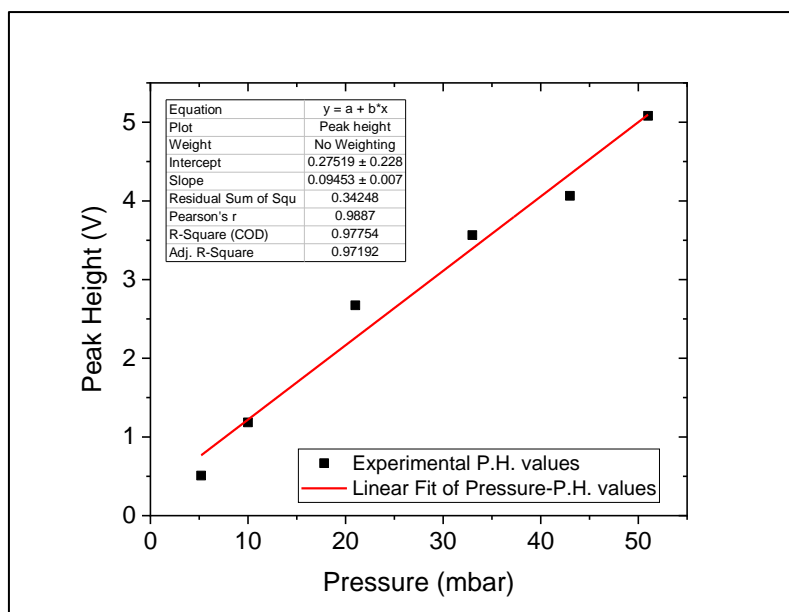
4.5.18 Least-squares regression line for NH_3 (TDLPAS)

❖ Ammonia (NH_3) – Hybrid TDLAS & TDLPAS

For the hybrid TDLAS-TDLPAS system, same peak as TDLPAS (6579.27 cm^{-1}) in both absorption and photoacoustic spectra was used for the Voigt fit and the extraction of peak height values (Fig 4.4.17). The least-squares regression lines for all measured values of pressure for both techniques are shown in Figures 4.4.19 and 4.4.20.



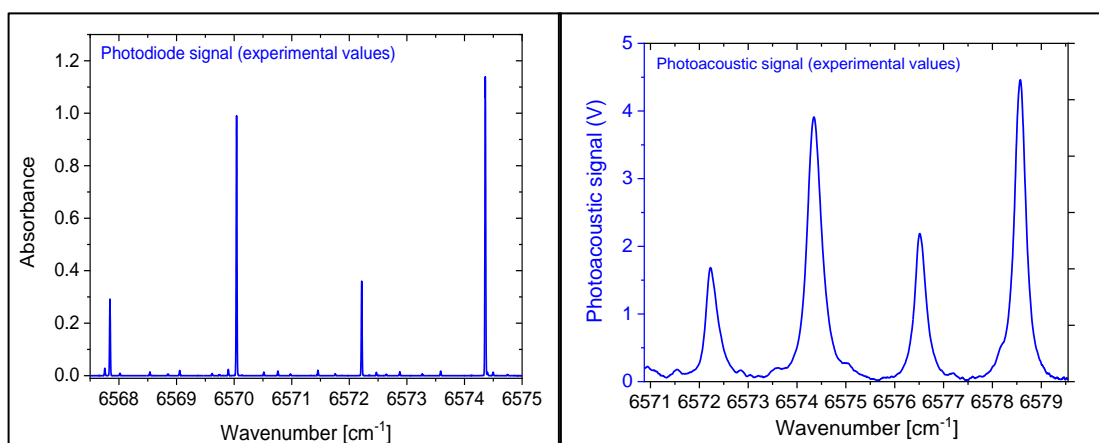
4.5.19 Least-squares regression line for NH_3 (TDLAS of hybrid system)



4.5.20 Least-squares regression line for NH_3 (TDLPAS of hybrid system)

4.6 Discussion

It is obvious from results shown in Table 1, that TDLAS in vacuum conditions presents best limits of detection for all gases probed. In TDLPAS, LLD for all gases shows a significant decrease. Broadening effects due to conditions of 1 bar total pressure of N_2 have altered the shape of narrow lines acquired in TDLAS (Fig. 4.6.1), also resulting in reduction of absorbance intensity.



4.6.1(Left) TDLAS experimental spectrum of C_2H_2 . (Right) TDLPAS experimental spectrum of C_2H_2 . Broadening effects have altered the lines' shape

Table 1. LLD of probed gases

<i>Spectroscopic technique</i> / <i>Probed gas</i>	<i>LLD (mbar)</i>		
	<i>TDLAS</i> (vacuum)	<i>TDLPAS</i>	<i>Hybrid</i> <i>TDLAS/TDLPAS</i>
<i>CH₄</i>	0.90669	-	-
<i>CO₂</i>	7.10124	13.51625	-
<i>C₂H₂</i>	0.23557	6.38171	-
<i>N₂O</i>	35.06181	97.43961	-
<i>NH₃</i>	0.46912	9.28624	11.03008/ 11.98716

Though, the most accurate comparison between efficiency of the two spectroscopic methods can be made for ammonia measurements in hybrid TDLAS/TDLPAS system, since measurements were conducted in same experimental conditions such as laser source (6578 cm⁻¹), pathlength of the gas cell and presence of N₂ buffer gas in the chamber. With comparable LLD obtained for both techniques, it is essential that we assess the potential and limiting factors of each one of them. TDLAS is undoubtedly a powerful, well-established, rapid, accurate method of detection with numerous applications. Along with other techniques such as DIAL (Differential Absorption LIDAR) or CRLAS (Cavity Ring-Down Laser Absorption Spectroscopy), have the potent of detection limits up to ppb levels. Still though, TDLPAS can be a useful tool for analysis as it may confront certain drawbacks of TDLAS as well as it can benefit from factors such as laser power and microphones number.

In TDLAS, photodetectors are manufactured to be active on certain responsivity areas depending on the lasers evolved. In that manner, measurements of different regions of electromagnetic spectrum (Vis-MIR-NIR) cannot be acquired with same photodetector. This issue can be resolved by the use of a microphone in TDLPAS, since this sensor is detecting pressure fluctuations (deriving from light and matter interaction) and not the light itself. Particularly in the case of MIR region, a microphone is an ideal solution for signal detection compared to highly expensive transducers, needed in TDLAS instead. Laser power is a deciding factor affecting differently the two techniques. TDLPAS benefits from high power lasers as photoacoustic signal is proportional to laser power, as can be seen from Equation 22[14], [17]:

$$V = aCS_M P_L c \quad (23)$$

where: V (Volt) is the photoacoustic signal, a (cm⁻¹ atm⁻¹) is the absorption coefficient at a given wavelength, C (Pa cm W⁻¹) the photoacoustic cell constant, S_M (V Pa⁻¹) the microphone responsivity, P_L (W) the cw laser power and c (atm) the trace gas concentration. On the contrary, high laser power of the incident light beam on a photodetector will often cause saturation effects. In TDLPAS measurements of CO₂, we exploited that fact by increasing the laser power 3 times the value set for TDLAS,

since carbon dioxide was the only gas measured with the exact same laser for both techniques.

Number of microphones can also be beneficial for the enhancement of signal in TDLPAS. The summation of the signals from a number m of single microphones results in a m -times higher effective photoacoustic signal because the total responsivity S_M is increased m -fold i.e.: $S_{M_{tot}} = m S_M$. On the other hand, noise increases only by \sqrt{m} [14].

5. Conclusions

In the current work, an experimental array was assembled in the lab for the investigation of gas matter under different spectroscopic methods. Five gases (CO_2 , CH_4 , C_2H_2 , NH_3 , and N_2O) were probed with two applied techniques (TDLAS and TDLPAS), by employing laser sources in the near-infrared region. A LLD (lower limit of detection) was obtained for the absorbing analytes, leading to the conclusion that TDLAS dominates over TDLPAS. Though, in the case of ammonia (measured in a hybrid TDLAS/TDLPAS system under same conditions) a more accurate evaluation between these techniques was made. Comparable values of ammonia LLD led to a discussion of advantages and disadvantages of the two methods and possible ways of improving measurement process and the results thereof. A motivation is created through current work for future analysis of more than one gas, with the hybrid spectroscopic system and a further application of these methods on liquid or solid state of matter. Also, a perspective of application of the techniques on food (olive oil, wine, vegetables etc.) volatile compounds is of great interest.

References

- [1] H. Sumizawa, H. Yamada, and K. Tonokura, "Real-time monitoring of nitric oxide in diesel exhaust gas by mid-infrared cavity ring-down spectroscopy," *Appl. Phys. B Lasers Opt.*, vol. 100, no. 4, pp. 925–931, 2010.
- [2] B. A. Paldus *et al.*, "Cavity ringdown spectroscopy using mid-infrared quantum-cascade lasers," *Opt. Lett.*, vol. 25, no. 9, p. 666, 2000.
- [3] M. W. Todd *et al.*, "Application of mid-infrared cavity-ringdown spectroscopy to trace explosives vapor detection using a broadly tunable (6–8 μm) optical parametric oscillator," *Appl. Phys. B Lasers Opt.*, vol. 75, no. 2–3, pp. 367–376, 2002.
- [4] F. Xin, J. Guo, J. Sun, J. Li, C. Zhao, and Z. Liu, "Research on atmospheric CO_2 remote sensing with open-path tunable diode laser absorption spectroscopy and comparison methods," *Opt. Eng.*, vol. 56, no. 6, p. 066113, 2017.
- [5] F. Zheng *et al.*, "Measurement of nitric oxide from cigarette burning using TDLAS based on quantum cascade laser," *Opt. Laser Technol.*, vol. 124, no. 2, 2020.
- [6] M. Norsuzila Ya'acob *et al.*, "We are IntechOpen, the world's leading publisher of Open Access books Built by scientists, for scientists TOP 1 %," *Intech*, vol. 32, pp. 137–144, 1989.
- [7] J. Li, K. Liu, W. Zhang, W. Chen, and X. Gao, "Carbon dioxide detection using NIR diode laser based wavelength modulation photoacoustic spectroscopy," *Opt. Appl.*, vol. 38, no. 2, pp. 341–352, 2008.
- [8] S. Alahmari, X. W. Kang, and M. Hippler, "Diode laser photoacoustic spectroscopy of CO_2 , H_2S and O_2 in a differential Helmholtz resonator for trace gas analysis in the biosciences and petrochemistry," *Anal. Bioanal. Chem.*, vol. 411, no. 17, pp. 3777–3787, 2019.
- [9] G. R. Lima, M. S. Sthel, M. G. Da Silva, D. U. S. Schramm, M. P. P. De Castro, and H. Vargas, "Photoacoustic spectroscopy of CO_2 laser in the detection of

- gaseous molecules,” *J. Phys. Conf. Ser.*, vol. 274, no. 1, 2011.
- [10] A. S. Franca and L. M. L. Nollet, *Spectroscopic Methods in Food Analysis*. 2017.
 - [11] M. Lackner, “Tunable diode laser absorption spectroscopy (TDLAS) in the process industries - A review,” *Rev. Chem. Eng.*, vol. 23, no. 2, pp. 65–147, 2007.
 - [12] J. Li, Z. Yu, Z. Du, Y. Ji, and C. Liu, “Standoff chemical detection using laser absorption spectroscopy: A review,” *Remote Sens.*, vol. 12, no. 17, pp. 1–44, 2020.
 - [13] A. Rosencwaig, *Photoacoustics and Photoacoustic Spectroscopy*. Wiley, New York, 1980.
 - [14] D. C. Dumitras, D. C. Dutu, C. Matei, A. M. Magureanu, M. Petrus, and C. Popa, “Laser photoacoustic spectroscopy: Principles, instrumentation, and characterization,” *J. Optoelectron. Adv. Mater.*, vol. 9, no. 12, pp. 3655–3701, 2007.
 - [15] A. Miklós, S. Schäfer, and P. Hess, “Photoacoustic Spectroscopy, Theory,” *Encycl. Spectrosc. Spectrom.*, pp. 2151–2158, 1999.
 - [16] J. P. Besson and L. Thévenaz, “Photoacoustic spectroscopy for multi-gas sensing using near infrared lasers,” *Lab. nanophotonique métrologie*, vol. Ph.D., no. Thèse No. 3670 (2006), pp. 1–189, 2006.
 - [17] S. Palzer, “Photoacoustic-based gas sensing: A review,” *Sensors (Switzerland)*, vol. 20, no. 9, 2020.
 - [18] M. Eck, “Performance enhancement of hybrid nanocrystal-polymer bulk heterojunction solar cells: aspects of device efficiency, reproducibility, and stability,” *Thesis Dr.*, pp. 1–217, 2014.
 - [19] G. A. West, J. J. Barrett, D. R. Siebert, and K. V. Reddy, “Photoacoustic spectroscopy,” *Rev. Sci. Instrum.*, vol. 54, no. 7, pp. 797–817, 1983.
 - [20] S. N. Thakur, “Photoacoustic Spectroscopy of Gaseous and Condensed Matter,” in *Photoacoustic Imaging: Principles, Advances and Applications*, 2019, pp. 1–21.
 - [21] Stanford Research Systems, “About Lock-In Amplifiers,” no. 408. Retrieved from; <http://www.thinksrs.com/downloads/PDFs/ApplicationNotes/AboutLIAs.pdf%0Apapers2://publication/uuid/D0353E29-AC61-45AE-A47E-51E0B32900FE>, pp. 1–9, 2004.
 - [22] P. Siozos, G. Psyllakis, P. C. Samartzis, and M. Velegrakis, “Autonomous Differential Absorption Laser Device for Remote Sensing of Atmospheric Greenhouse Gases,” *Remote Sens.*, vol. 14, no. 3, p. 460, 2022.
 - [23] A. Campargue *et al.*, “Overtone spectroscopy in nitrous oxide,” *J. Chem. Phys.*, vol. 103, no. 14, pp. 5931–5938, 1995.
 - [24] J. K. Valiunas, G. Stewart, and G. Das, “Detection of nitrous oxide (N₂O) at sub-ppmv using intracavity absorption spectroscopy,” *IEEE Photonics Technol. Lett.*, vol. 28, no. 3, pp. 359–362, 2016.
 - [25] I. D. All, V. Modes, and S. First, “Determining the Normal Modes of Vibration,” vol. 1, no. 2, pp. 1–10.
 - [26] M. E. Webber, D. S. Baer, and R. K. Hanson, “Ammonia monitoring near 15 μ m with diode-laser absorption sensors,” *Appl. Opt.*, vol. 40, no. 12, p. 2031, 2001.
 - [27] H. Deng, J. Sun, B. Yu, and J. Li, “Near infrared diode laser absorption spectroscopy of acetylene between 6523 and 6587 cm⁻¹,” *J. Mol. Spectrosc.*, vol. 314, pp. 1–5, 2015.
 - [28] R. El Hachtouki and J. Vander Auwera, “Absolute line intensities in acetylene:

- The 1.5- μm region,” *J. Mol. Spectrosc.*, vol. 216, no. 2, pp. 355–362, 2002.
- [29] G. B. Armen, “Infrared spectroscopy of acetylene,” pp. 1–34, 2007.
- [30] C. E. Miller and L. R. Brown, “Near infrared spectroscopy of carbon dioxide I. $^{16}\text{O}^{12}\text{C}^{16}\text{O}$ line positions,” *J. Mol. Spectrosc.*, vol. 228, no. 2 SPEC. ISS., pp. 329–354, 2004.
- [31] M. Buback, J. Schweer, and H. Tups, “Near Infrared Absorption of Pure Carbon Dioxide up to 3100 bar and 500 K. I. Wavenumber Range 3200 cm^{-1} to 5600 cm^{-1} ,” *Zeitschrift fur Naturforsch. - Sect. A J. Phys. Sci.*, vol. 41, no. 3, pp. 505–511, 1986.
- [32] S. Kassi, B. Gao, D. Romanini, and A. Campargue, “The near-infrared (1.30–1.70 μm) absorption spectrum of methane down to 77 K,” *Phys. Chem. Chem. Phys.*, vol. 10, no. 30, pp. 4410–4419, 2008.
- [33] O. N. Ulenikov, E. S. Bekhtereva, S. Albert, S. Bauerecker, H. M. Niederer, and M. Quack, *Survey of the high resolution infrared spectrum of methane ($^{12}\text{CH}_4$ and $^{13}\text{CH}_4$): Partial vibrational assignment extended towards $12\,000\text{ cm}^{-1}$* , vol. 141, no. 23. 2014.
- [34] A. V. Nikitin, M. Rey, and V. G. Tyuterev, “Accurate line intensities of methane from first-principles calculations,” *J. Quant. Spectrosc. Radiat. Transf.*, vol. 200, pp. 90–99, 2017.
- [35] E. S. Barr and C. H. Chrisman, “The absorption spectra of sugars in the near infra-red,” *J. Chem. Phys.*, vol. 8, no. 1, pp. 51–55, 1940.
- [36] Wikipedia, “Molecular energy levels.” [Online]. Available: https://commons.wikimedia.org/wiki/File:Molecular_energy_levels_en.svg.
- [37] LibreTexts, “Rotations Accompany Vibrational Transitions.” [Online]. Available: [https://chem.libretexts.org/Bookshelves/Physical_and_Theoretical_Chemistry_Textbook_Maps/Physical_Chemistry_\(LibreTexts\)/13%3A_Molecular_Spectroscopy/13.02%3A_Rotations_Accompany_Vibrational_Transitions](https://chem.libretexts.org/Bookshelves/Physical_and_Theoretical_Chemistry_Textbook_Maps/Physical_Chemistry_(LibreTexts)/13%3A_Molecular_Spectroscopy/13.02%3A_Rotations_Accompany_Vibrational_Transitions).
- [38] J. F. Kielkopf, “New approximation to the Voigt function with applications to spectral-line profile analysis,” *J. Opt. Soc. Am.*, vol. 63, no. 8, p. 987, 1973.
- [39] D. J. Anderson, “Determination of the lower limit of detection,” *Clin. Chem.*, vol. 35, no. 10, pp. 2152–2153, 1989.